Evolution of deformation twinning mechanisms in magnesium from low to high strain rates

Nicolò Della Ventura, Amit Sharma, Szilvia Kalácska, Manish Jain, Thomas E.J. Edwards, Cyril Cayron, Roland Logé, Johann Michler, Xavier Maeder

Materials & Design 217 (2022) 110646

Contents lists available at ScienceDirect

Materials & Design

journal homepage: www.elsevier.com/locate/matdes

Evolution of deformation twinning mechanisms in magnesium from low to high strain rates

Nicolò M. della Ventura [a,*], Amit Sharma [a], Szilvia Kalácska [a], Manish Jain [a], Thomas E.J. Edwards [a], Cyril Cayron [b], Roland Logé [b], Johann Michler [a], Xavier Maeder [a]

[a] Empa, Swiss Federal Laboratories for Materials Science and Technology, Laboratory for Mechanics of Materials and Nanostructures, Feuerwerkerstrasse 39, 3602, Thun, Switzerland
[b] Laboratory of ThermoMechanical Metallurgy (LMTM), PX Group Chair, Ecole Polytechnique Fédérale de Lausanne (EPFL), Rue de la Maladière 71b, 2000 Neuchâtel, Switzerland

HIGHLIGHTS

- The evolution of the twinning mechanism was experimentally investigated from low to high strain rates at the micron-scale.
- The competition of twinning dislocations and pyramidal dislocations allows the evolution of the twin boundary along a non-invariant twin plane.
- At high strain rates, the prismatic to basal plane conversion resulting in a 90° lattice reorientation governs the entire twin process.
- The 3D reconstruction of the twins allows to fully assess the spatial geometry of the twin boundaries.
- The boundary lateral to the shear direction of deformation twins was investigated at different strain rates at the micron-scale.

GRAPHICAL ABSTRACT

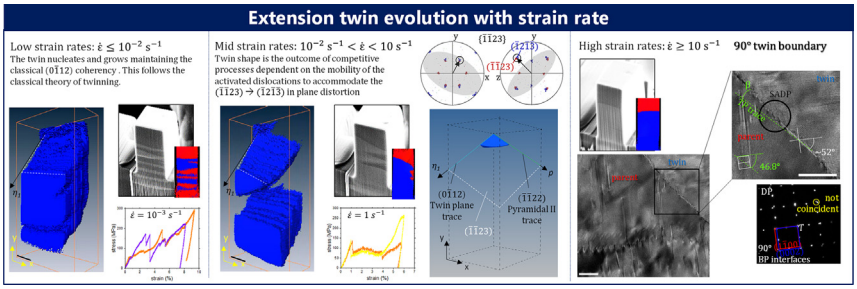

ARTICLE INFO

Article history:
Received 14 January 2022
Revised 30 March 2022
Accepted 7 April 2022
Available online 12 April 2022

Keywords:
Magnesium
Deformation twinning
Twin interface
High strain rate
Micropillar compression

ABSTRACT

We present a systematic investigation of {10$\bar{1}$2} extension twinning mechanism in single crystal magnesium micropillars deformed over seven orders of magnitude of strain rate, from 10^{-4} to 500 s^{-1}, revealing how the accommodation of newly formed twins evolves with and depends on the kinetic compatibility of interfacial processes when high deformation rates are imposed. By combination of post-mortem 3D Electron Backscattered Diffraction, Transmission Kikuchi Diffraction and Transmission Electron Microscopy techniques, this work unveils the progressive evolution of the accommodating twin mechanisms from low to high strain rate, correlating differences in mechanical behavior with differences in twin crystallography. Away from quasi–static conditions, simple considerations of twinning shear do not suffice to describe unconventional twin morphologies, requiring the competition between newly activated dislocations and lattice distortions for allowing the evolution of the twin boundary along non–invariant twin planes. Under shock compressions, the basal/prismatic transformation establishing a lattice misorientation of 90° entirely governs the parent → twin conversion. The results illustrated here confirm

* Corresponding author.
E-mail addresses: nicolo.dellaventura@empa.ch (N.M. della Ventura), amit.sharma@empa.ch (A. Sharma), szilvia.kalacska@empa.ch (S. Kalácska), manish.jain@empa.ch (M. Jain), thomas.edwards@empa.ch (T.E.J. Edwards), cyril.cayron@epfl.ch (C. Cayron), roland.loge@epfl.ch (R. Logé), johann.michler@empa.ch (J. Michler), xavier.maeder@empa.ch (X. Maeder).

https://doi.org/10.1016/j.matdes.2022.110646

that some of the recent interpretations deduced by particular twin morphologies are not universally valid and that deformation twinning is not only stress- but also strongly time–controlled.

1. Introduction:

Deformation twinning (DT) has a very important role in accommodating plastic deformation in hexagonal–close–packed (HCP) metals due to the limited number of "easy" slip systems [1–3]. However, DT is known to be associated with a lack of ductility, limited machinability, and cracking [3–6], which affect the industrial applicability of these metals and make them only partially competitive compared to other light metal alloys [7]. Nevertheless, magnesium (Mg) and its alloys are still recognized as lightweight structural materials with potential application in the automotive or aerospace industry due to their exceptional high strength–to–weight ratio [8]. Therefore, Mg has attracted immense interest from the scientific community over the last decade, pushing investigations into the fundamental understanding of DT in HCP metals, such as nucleation and propagation mechanisms [9].

Although the development and use of various types of Mg–based alloys with a good strength and ductility combination have been achieved over the years, the phenomenon of DT is still not completely understood [9–14]. Classically, the most commonly observed $\{10\bar{1}2\}$ twin in Mg can be described in its final state as an 86.4° rotation of the parent grain across the crystallographic *a*–axis (Fig. 1a), resulting from a complex shear–shuffle mechanism [1]. We remind that when the primitive unit cell contains more than one atom (two for HCP), shear and atomic shuffling are both necessarily involved to restore the crystal lattice in a mirrored configuration, as the simple shear does not suffice to carry all the atoms into their correct final positions [13]. The conventional parent–twin interface (i.e. the twin boundary, TB), due to strain compatibility conditions, is expected to develop along the $\{10\bar{1}2\}$ invariant twin plane, K_1 (Fig. 1a). We will therefore refer to it as a (86.4°, *a*) twin. Nevertheless, major controversies have arisen from numerous experimental observations of "unconventional" twinning features presented as counterexamples of the centenary classical theory, such as the occurrence of non–invariant parent–twin interfaces [15], like the prismatic–basal (PB/BP) serrations [12,16,17]; the finding of 90° misoriented parent–twin interfaces across the crystallographic *a*–axis (Fig. 1b) interpreted as a proof of an unfulfilled classical simple shear [18,19]; the non–Schmid factor behavior [20] of twinning and other "anomalous" aspects [9,21]. From this, the main debates are based on disagreements between heterogeneous and homogeneous theories that aim to justify the precise atomic trajectories that govern the parent → twin transformation [13]. The former focuses on the key role of special twin boundary dislocations called twinning dislocations (TDs) in mediating the twinning processes [22–25], whereas the latter describes DT as a collective movement of atoms without involving TDs [12,18,26].

In this context, we report a micropillar compression investigation on single-crystal pure Mg performed over seven orders of magnitude of strain rate ($\dot{\varepsilon}$) to progressively compare the nature of the deformations from quasi–static to shock compressions at room temperature. At small scales and under high strain rate (HSR) loading, we expect that the character and mobility of defects assisting DT are strongly influenced by both the high–stress environment and changes in the kinetic compatibility of lattice distortions when a rapid transition of the atoms' positions is externally imposed. The description of the evolution of the mechanisms accompanying DT is presented, unveiling important aspects for the fundamental comprehension of twinning in HCP metals.

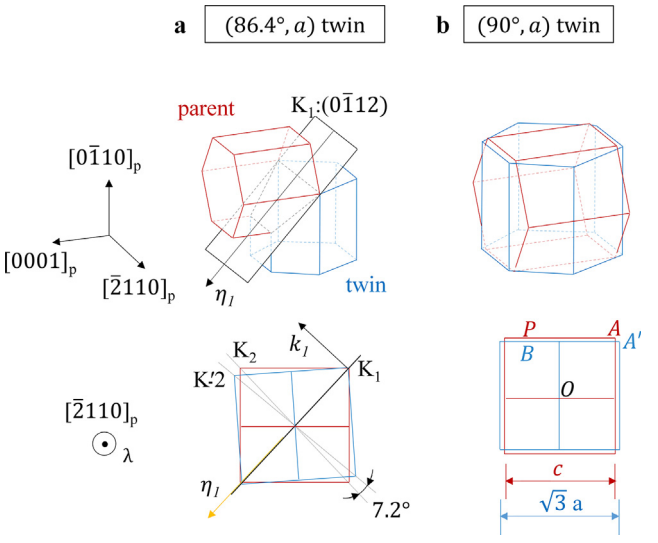

Fig. 1. Schematic illustration of the conventional (86.4°, *a*) twin and the unconventional (90°, *a*) twin geometries. (**a**) K_1 defines the twin plane, k_1 the normal to the twin plane, η_1 the twinning shear direction and λ the cross product $k_1 \times \eta_1$. K_2 represents the conjugate twinning plane that transforms into K'_2 because of the shear. (**b**) The reoriented lattice does not hold a rigorously crystallographic (rational) orientational relationship with the parent lattice as expected for twinning. A and A' do not coincide.

2. Materials and methods

2.1. Experimental characterization

A 99.999% pure, fully single–crystalline Mg sample (PSC, Easton, USA) was mechanically polished and subsequently electro–polished at 12 V with a refrigerated (10 °C) electrolyte, comprised of 85 % ethanol, 5 % HNO_3 and 10 % HCl. The sample was then used for squared pillar fabrication using Ga^+ Focused Ion Beam (FIB) (Tescan, Lyra3). The square cross–section pillar dimensions (5x5x10 μm^3, see Fig. 2a) were chosen so that a width–to–height aspect ratio of 1:2 was achieved. The pillar taper, caused by inherent limitations of the FIB milling procedure, was found to be on average 1–2° and the surfaces showed almost no curtaining artifacts. Details on the measures taken to fabricate the structures and minimize the potential FIB artifacts are shown in Fig. S.1 in Supplementary material. The pillar top was used to measure the area from which the engineering stress was calculated. Stresses and strains (σ, ε) are nominal. The pillars were fabricated at the front surface of the bulk sample, allowing for Electron Backscattered Diffraction (EBSD) acquisitions before and after the deformation. The structures were then compressed with a nanoindenter fitted with a 20 μm diameter flat punch. The micromechanical tests were conducted using a dedicated *in situ* Alemnis AG nanoindenter set–up for quasi–static and HSR conditions [27] mounted inside a Scanning Electron Microscope (SEM, Philips XL30). The set-up employs a piezo-electric load sensor at strain rates $\geq 1\ s^{-1}$ and a standard strain gauges-based load cell below.

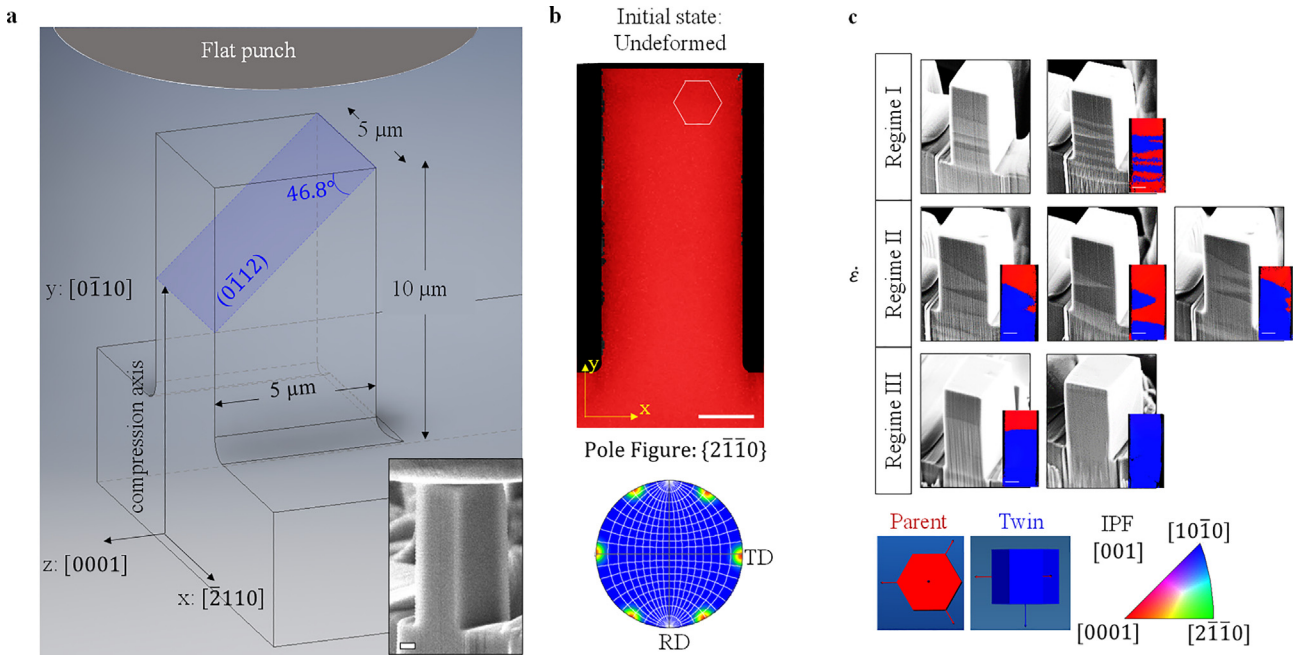

Fig. 2. (**a**) Overview of the experimental configuration adopted, together with an SEM image of an undeformed pillar. (**b**) EBSD map and related {2 $\bar{1}$ $\bar{1}$ 0} pole figure showing the initial crystallographic orientation. RD. Rolling Direction, TD. Transversal Direction. (**c**) Secondary electron images of some pillars deformed within the three different strain rate regimes. The images have been saturated so that the parent domain appears darker, the twin domain brighter. A change in the parent–twin interface inclination is visible in Regime II. Some respective EBSD maps are shown (parent domain in red and twin domain in blue, as per legend). Eventual slight discordances between the EBSD maps and correspondent SEM images are due to FIB polishing performed after unloading to improve the EBSD quality. The inverse pole figure (IPF) color code in all maps indicates the crystal orientation in the out-of-plane direction (normal direction, ND). ND corresponds to the z–axis in (**a**), TD to the x–axis and RD accordingly. All scale bars correspond to 2 μm length.

2.2. EBSD acquisitions and 3D EBSD reconstructions

All EBSD maps were acquired inside a field emission gun (FEG) SEM (Tescan, Lyra3) with a Symmetry detector and Aztec 4.2 software (Oxford Instruments, UK), under 20 kV, 10nA beam conditions and a 100 nm step size, using a 2 × 2 binning (622 × 512 px^2). As EBSD is a surface technique, the three–dimensional reconstruction of the shape and distribution of the twins formed upon loading was performed by coupling post mortem 2D EBSD acquisitions with FIB tomography in a static setup [28,29] (see later). The 2D EBSD maps were captured after every FIB slice of 200 nm from the front surface through the thickness of the pillars. FIB slicing was done at 30 kV and 100 pA. After the EBSD evaluation, Photoshop CC 2017 was used to manually align the slices by changing the visibility of one slice over the other. The Amira v5.2 software was then used to form the 3D reconstructions from the 2D maps.

2.3. TKD and TEM analysis

To investigate and analyze the atomic structure of the different TBs, several deformed pillars were lifted out and furtherly thinned down to ∼ 100 nm. The [$\bar{2}$ 110] direction (i.e. the *a*–axis), being the rotation axis of the {10 $\bar{1}$ 2} twin, was selected to be the zone axis (Z.A.). The atomic resolution images were acquired using a ThermoFischer Themis 200 G3 spherical aberration (probe) corrected Transmission Electron Microscope (TEM) operating at 200 kV. A double tilt sample holder was used to achieve various zone axis conditions. The dislocation types were determined based on diffraction contrast analysis criteria (see Table S.1 in Supplementary material) by analyzing the bright-field (BF) and weak-beam dark-field (WBDF) images. In some cases, the TEM thin foils were mapped using the Transmission Kikuchi Diffraction (TKD) technique to provide an overview of the parent and twin domains viewed from the lateral side of the pillars. For this, an electron beam of 30 kV and 10nA was used. It is important to note that any in–plane rotation of the parent crystal in the TEM or TKD images shown in this article is simply the result of the manual positioning of the foil in the microscopes.

3. Results

Several pillars were compressed along the [0 $\bar{1}$ 10] crystal direction in displacement–rate controlled mode for each strain rate condition, from 10^{-4} s^{-1} to 500 s^{-1}. The coordinate system used in this work is reported in Fig. 2a. The stress–strain (σ–ε) curves and videos related to the *in situ* tests can be found in Fig. 3 and Supplementary videos, respectively. The initial sample orientation was checked for all the structures using EBSD (Fig. 2b) ensuring an orientation accuracy of ∼ 0.5°. This specific orientation was selected for favoring extension twin formation induced by the stretch of the crystal along the *c*–axis [30].

3.1. {10 $\bar{1}$ 2} twin morphologies vs strain rates

Thermodynamically speaking, the energy that needs to be given to the system to induce twinning nucleation has to overcome the energy associated with the formation of a new interface, i.e. the TB. Thus, once reaching the critical resolved shear stress for twinning (τ^{T}_{CRSS}), the overall energy of the system is reduced through energy dissipation. In displacement–controlled conditions the twin transformation process leads to a significant load drop in the σ–ε curves, as observed in our recent work [29]. Additionally, upon twin nucleation and under a continuously applied deformation condition, the predominance of the twin propagation process in accommodating the plastic deformation is usually manifested by a plateau of σ, where a small increase in stress results in a signif-

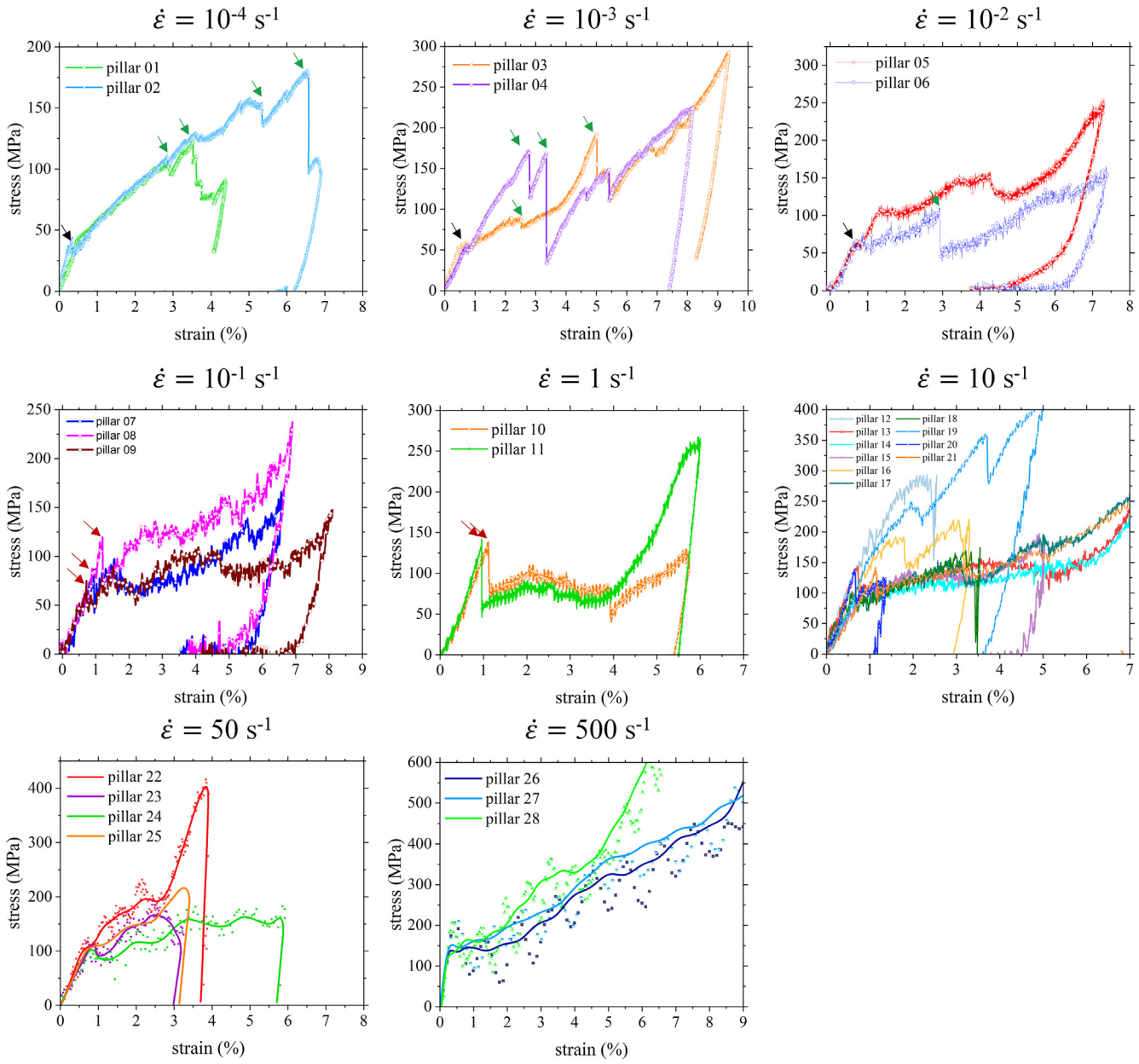

Fig. 3. Stress–strain curves at the different imposed strain rates. Two or more pillars were tested in each condition. A higher number of pillars have been used for high strain rate testing (Regime III). At greater than $10\dot{\varepsilon}$ s^{-1}, the flow stress starts exhibiting oscillations due to the resonance frequency of the system [27]. The material response is overwhelmed by the oscillation amplitude, not allowing a precise extraction of the material properties. Adjacent average smoothing procedure every 5 and 35 data points for 50 and 500 s^{-1} respectively has been therefore adopted. Sampling rate. 100 kHz and 1 MHz, respectively.

icant increase in strain [31,32]. The changes observed in the microstructures (progressively described in this work) and consequently in the mechanical responses (Fig. 3 and Fig. 4) at different strain rates allow us to define three different regimes: Regime I (low strain rates), $\dot{\varepsilon} \leq 10^{-2}s^{-1}$; Regime II (mid–strain rates), $10^{-2}s^{-1} < \dot{\varepsilon} < 10s^{-1}$; Regime III (high strain rates), $\dot{\varepsilon} \geq 10s^{-1}$ (see Fig. 4).

- In Regime I, the onset of the plastic deformation (yield stress, σ_y) is observed by a stress plateau (black arrows in Fig. 3) usually followed later by a significant load drop (twin transformation process, green arrows in Fig. 3) at larger deformation. It is important to point out that the magnitude of the load drop associated to the twin occurrence strongly depends on the initial volume of the crystal that undergoes the parent → twin transformation. Especially at low strain rates, this can vary according to the complex local strain field that develops in the first few-hundred nanometers underneath the pillar–indenter contact surface. Nevertheless, from Fig. 3 it appears that deformation by twinning mainly manifests at ∼ 3% of strain. After the evolution of the twin domain, the σ–ε curves show a continuous strain hardening likely induced by the activation of harder slip systems inside the twin domains (Fig. 5), as well as twin–twin, dislocation–twin, and dislocation–dislocation interactions [6,33–35]. The pole figures (PF) obtained from the EBSD maps reveal consistently the formation of one $\{10\bar{1}2\}$ twin variant, i.e. $(0\bar{1}12)$. In the classical definition of twins, this implies that the TB develops following the twin habit plane geometry (blue–colored) as shown in Fig. 2a, which translates

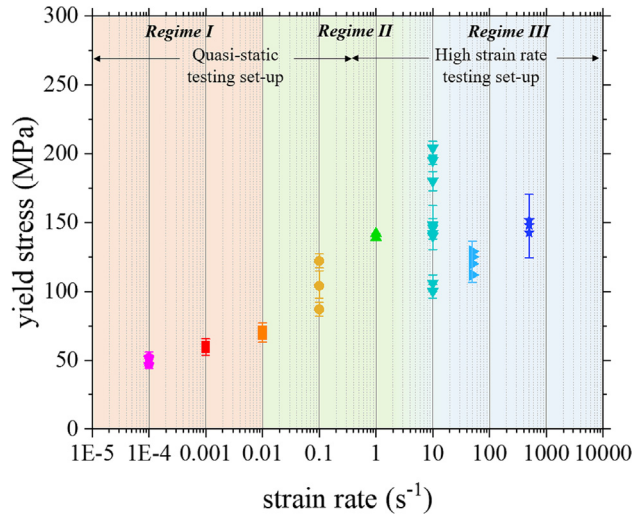

Fig. 4. Yield stress vs strain rate. Regimes I, II, and III are defined based on the change in material response.

to a TB that appears 0° and 46.8° inclined to the horizontal direction when viewed in the *xy* and *yz* planes, respectively (see Fig. 2c and Fig. 5).

- In Regime II, unlike Regime I, it appears that the twin nucleation (load drop) establishes the onset of plastic deformation (red arrows in Fig. 3). The yield stress is then measured accordingly. The σ–ε curves report a significant stress plateau right after the elastic regime, followed by strain hardening. This suggests that upon nucleation the twin propagation process accommodates most of the plastic deformation. Here, additionally, the majority of the TBs deviate from the $(0\bar{1}12)$ twin plane in the *xy* plane, as shown in Fig. 6a, appearing inclined to the horizontal direction. The same result was systematically observed at mid–strain rates on the *xy* surface of other pillars (Fig. 2c). This particular twin feature can be caused either by 1) the change in the $\{10\bar{1}2\}$ twin process from Regime I to Regime II that eventually leads to the development of an "unclassical" $(0\bar{1}12)$ TB or 2) the activation of other twin modes. Interestingly, initial analysis of the EBSD measurements showed that the twins were characterized by an 86.4° rotation around the *a*-axis, as for the $\{10\bar{1}2\}$ twin. One would then reasonably suppose that despite the "unconventional TB", 1) is more likely than 2). Further considerations will be presented later.
- In Regime III, the spatial geometry of the emerging twin variant commutes once more at HSR as shown in Fig. 2c. From the analyses of TEM images and TKD orientation maps (see Fig. 7, Fig. 8 and Fig. S.2), the TBs in the *yz* plane appear highly incoherent and a consistent 90° misorientation was observed across the parent–twin interfaces. Here, at $\dot{\varepsilon} = 10s^{-1}$, a stochastic material response shown by variable yield stress values was detected compared to that in Regime I and II (Fig. 3 and Fig. 4). Notably, at $\dot{\varepsilon} > 10s^{-1}$, the oscillation frequency of the system begins to appear in the material response. This is especially critical in soft metals as Mg, where the plasticity occurs within few–hundred MPa, limiting the precise extraction of the yield stress as the actual material behavior is overwhelmed by the resonant frequency of the system [27]. Consequently, the yield stress values have been measured by the averaged curve from the recorded data points (Fig. 3), as usually adopted [36–38], and higher error bars have been considered accordingly (Fig. 4). Most importantly though is that, despite the calculated yield stress values have undoubtedly higher degree of uncertainty due to the significant complexity of the experiment, no remarkable increments of σ_y are however seen at high strain rates. To further correlate the nature of the deformation and the microstructural evolution to the mechanical response of the material, TEM observations have been performed.

The interpretation of the accommodating twin processes in the three regimes is presented hereafter.

3.2. Three–dimensional $\{10\bar{1}2\}$ twin geometry at low and mid–strain rates

For sake of clarity, we decide to use in this work the following vocabulary recently adopted [39] to help to distinguish two particular projections of the twin domain: the "Bright Side" (BS) and the "Dark Side" (DS), representing the view along λ (i.e. the x–axis) and the view along η_1 (the shear direction), respectively (Fig. 9). The BS of the $\{10\bar{1}2\}$ twin in Mg has been widely investigated as it contains the k_1 and η_1 directions of propagation, of high interest for understanding the motion of TDs on alternating K_1 planes. On the contrary, despite recent exceptions [29,40–44], the DS still has not been sufficiently investigated experimentally as such projection is reported to be, in principle, "crystallographically unobservable" [39]. Here, however, we assessed the spatial evolution of the twin grains of some deformed structures through a 3D EBSD reconstruction (Fig. 9a, 9b, Fig. S.3, S.4 and S.5, and videos), shedding light on the morphology of the twin domain from both the BS and DS at the micron scales, resulting from different strain rate compressions. In particular, we focused our attention on Regime I and Regime II to delve into the changes of the twin morphology described before. It is important to point out that the 3D domains obtained in both regimes are of high interest as 1) their growth has not been affected by the presence of grain boundaries; 2) they belong to "adult" twins, revealing how the facets expand as the twins become larger. The latter point is often questioned as molecular dynamic (MD) simulations are limited to twin volumes of few thousand nm^3 and the HSR tests on bulk Mg [45] develop twins of thousand μm^3. Hence, eventual changes in the twin shapes depend on and can be addressed to the different character and mobility of the lattice dislocations and the possible activation of other slip/twin modes caused by the changes in the kinetics of atomic rearrangements and consequent evolution of the facets that constitute the twin domain.

Fig. 9a and 9b illustrate the obtained distribution of the nucleated twin crystals in two compressed pillars (respectively of Regime I and II) observed from three viewpoints around the longitudinal axis. The 3D reconstructions show that the twin domain develops along the $(0\bar{1}12)$ twin plane in Regime I (Fig. 9a). This is confirmed by the inclinations of the TB in the *xy* and *yz* planes with the horizontal, 0° and 46.8° respectively. The classical $\{10\bar{1}2\}$ extension twinning thus governs the plastic deformation at low strain rates. The corresponding BS and DS views are illustrated in Fig. 9c. In Regime II, the systematic 26°–32° inclination of the TB (visible in the *xy* twin plane as shown in Fig. 6a, Fig. 9b and Fig. S.4, S.5) is well maintained throughout the thickness of the structure (i.e. along *z*). However, in the *yz* plane, the TB shows a 46.8° inclination with the horizontal, parallel to the trace of the $(0\bar{1}12)$ twin plane (see Fig. 9d). The 3D reconstruction thus reveals similar twin shapes in the BS view between the two regimes but different twin evolutions when observed from the DS view (Fig. 9c–d).

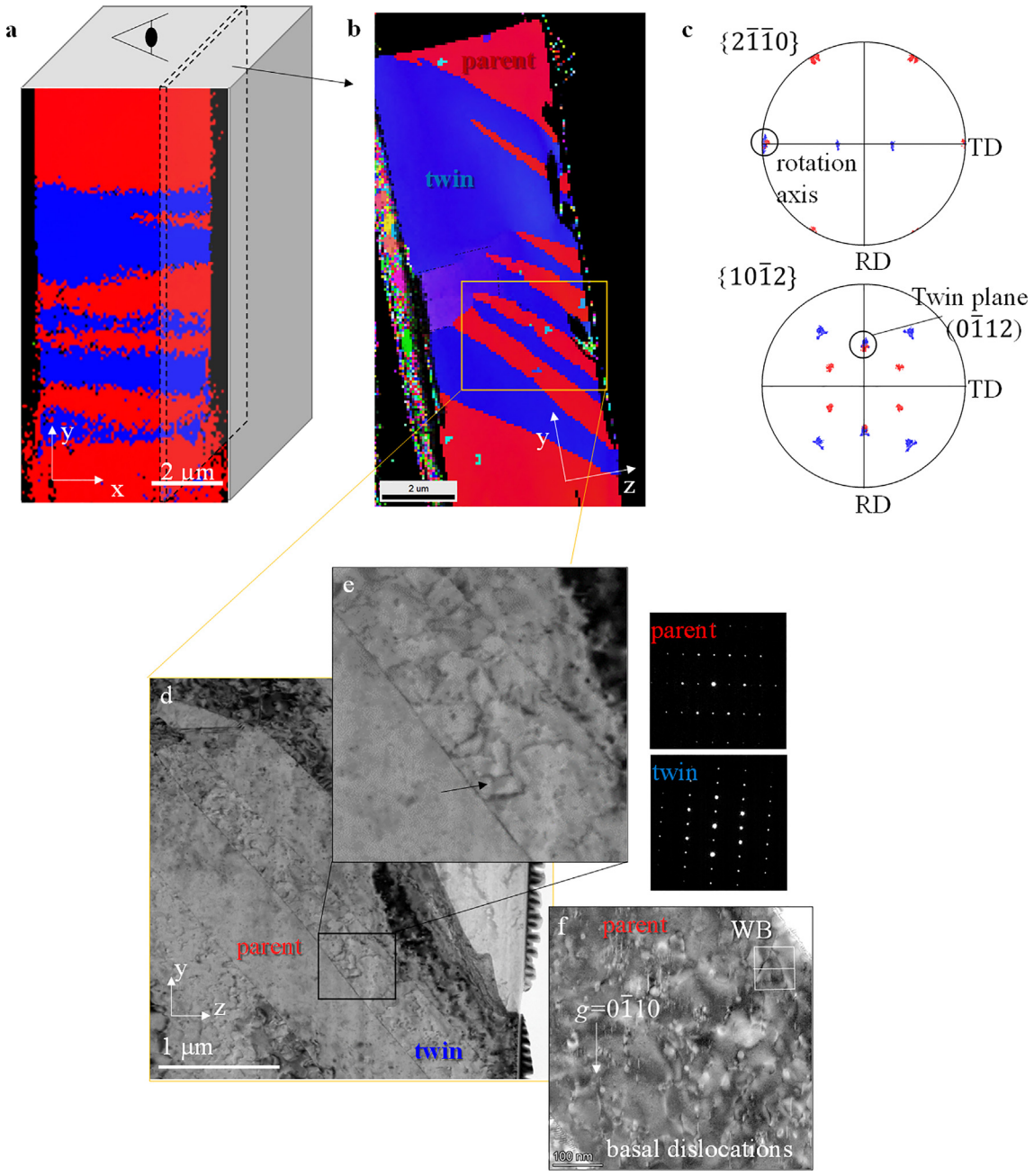

Fig. 5. Frontal (*xy* plane) and lateral (*yz* plane) view of a 7% strained pillar deformed at $\dot{\varepsilon} = 10^{-3}\ s^{-1}$ (Regime I). The reference system is associated with that in Fig. 2a. (**a**) EBSD map on the front surface. (**b**) TKD map showing the twin and parent phases. (**c**) Pole Figures related to the EBSD map in (**a**) showing the occurrence of (0 $\bar{1}$ 12) twin. RD. Rolling Direction (along *y*), TD. Transversal Direction (along *x*). (**d–f**) BF and WBDF TEM images for the pillar shown in (**b**). Because of extension twinning, the crystal undergoes a crystallographic reorientation that places the *c*-axis almost parallel to the loading direction. With proceeding strain, subsequent accommodation of plastic deformation can occur through activation of secondary (harder) deformation modes, particularly in the twins themselves, where < c + a > dislocations were detected (black arrow) (**e**). (**f**) In the parent domain, limited basal slip activity is detected, however, due to the zero Schmid factor imposed by the chosen orientation, it does not result to be the main mode of deformation. The twin interface appears to conform to the classical (0 $\bar{1}$ 12) twin plane geometry. The crystal misorientation was found to be 86.4° around the *a*–axis (see the diffraction pattern), in line with that for conventional {10 $\bar{1}$ 2} twins.

4. Discussion

4.1. Twin mechanism at low strain rates

In Regime I, the stress plateau and the strain hardening precede the onset of the twin mechanism (Fig. 3). This suggests that the formation of a twin nucleus of finite size occurs upon the activity of < a > dislocations underneath the pillar–indenter contact region, similar to what has been largely observed in Mg during direct and indirect *c*–axis extension at low strain rates [29,35,46]. The pillar tapering of ~ 1-2° makes the top–back edge of the structures the principal twin initiation site (see Fig. 9a). As the resolved shear stress along the [01$\bar{1}$1] twin direction is positive, the predominance of the (0$\bar{1}$12) twin variant is thus justified. The twin growth proceeds to maintain the original (0$\bar{1}$12) coherency (see Fig. 9a, c).

4.2. Twin mechanism at mid strain rates

From the 3D reconstruction (Fig. 9b, d), the Miller indices associated to the crystallographic twin plane along which the twin

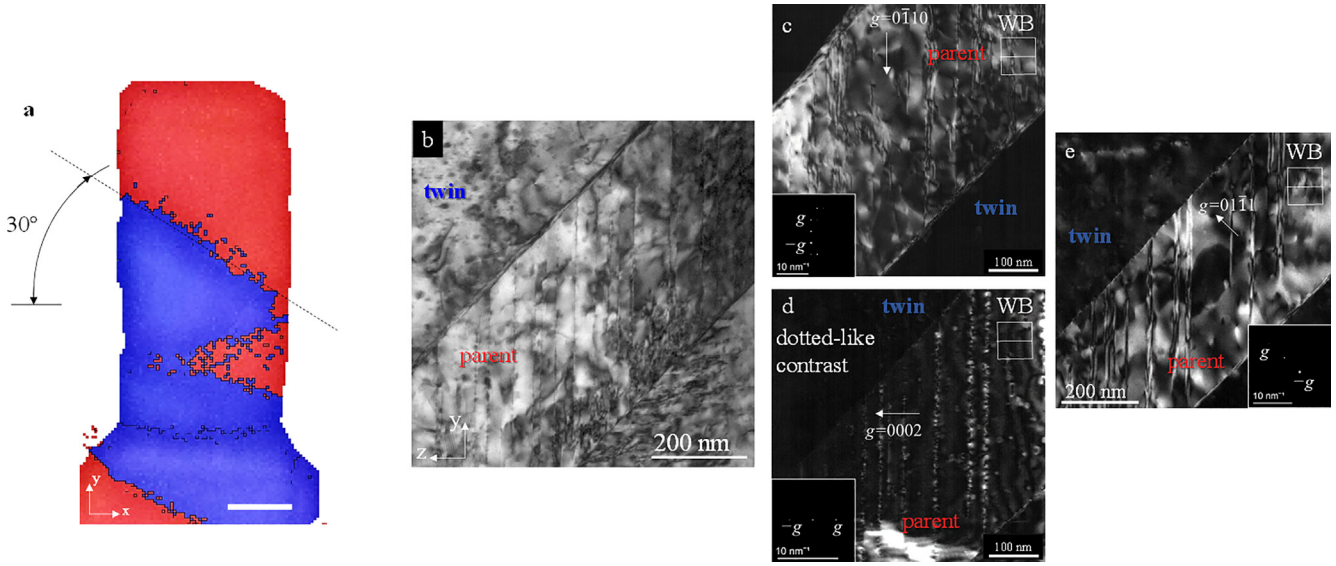

Fig. 6. (**a**) EBSD map of a 5.2% strained pillar deformed at $\dot{\varepsilon} = 1\ s^{-1}$ (Regime II) showing a 30° inclined twin boundary in the *xy* plane. Scale bar. 2 μm. BF (**b**) and WBDF (**c**-**e**) images inside the parent domain associated with the (0002), (0 1 $\bar{1}$ 0) and (01 $\bar{1}$ 1) diffraction spots. The character of the activated dislocation types was investigated in Region II based on diffraction contrast analysis criteria (requiring the use of Table S.1) and is discussed in Paragraph 4.4.

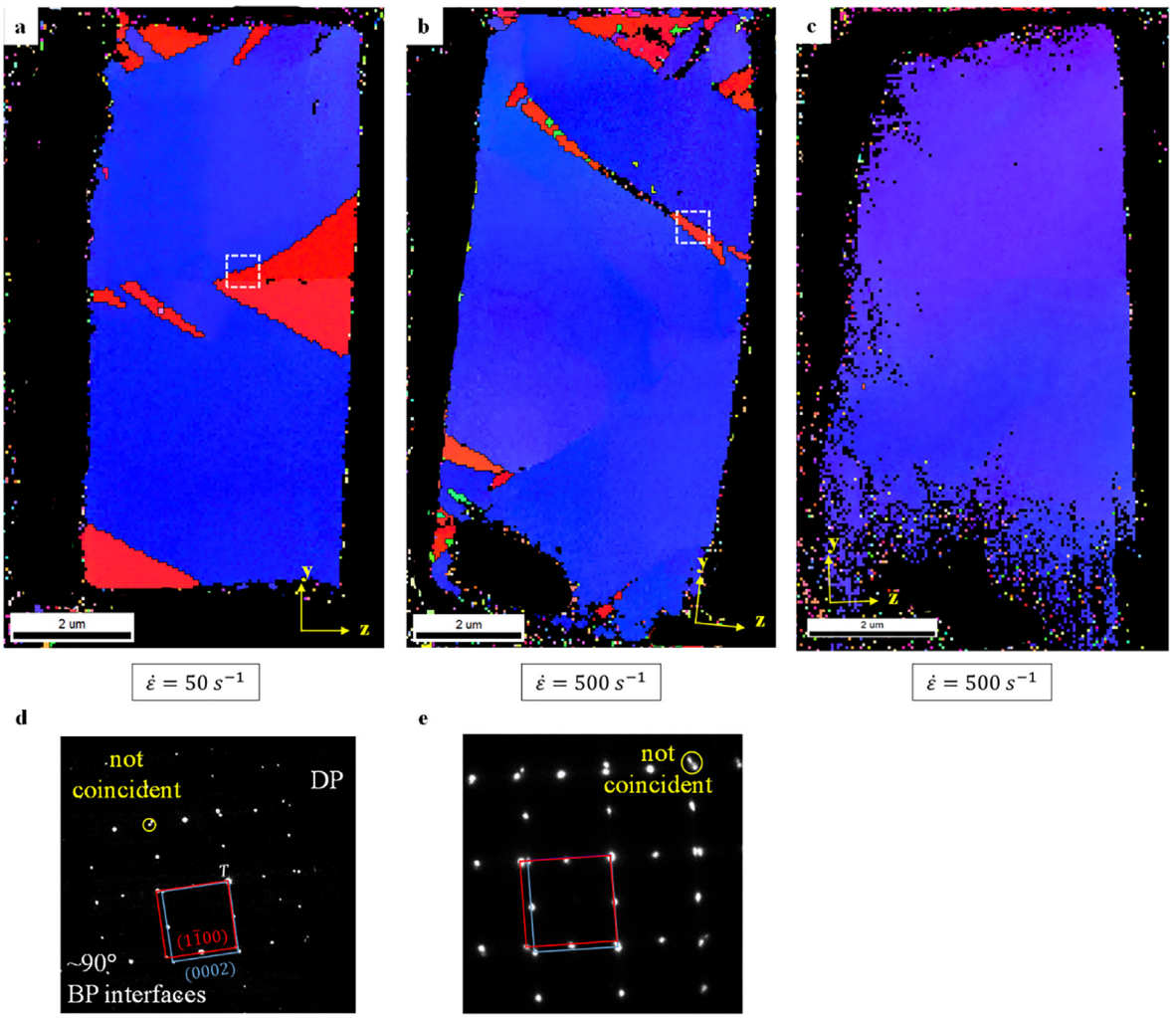

Fig. 7. TKD maps (lateral views) of three structures deformed in Regime III. The reference system is associated with that in (Fig. 2a). Twin domain in blue and parent domain in red. (**a**-**c**) As can be observed from the TKD maps, almost all the structures' volumes have undergone a crystallographic reorientation from the parent into the twinned domain. The majority the TBs are characterized by 90° BP interfaces that grow locally very incoherently. (**d**,**e**) Selected Area Diffraction Patterns associated with the regions highlighted by the dashed squares in (**a**) and (**b**).

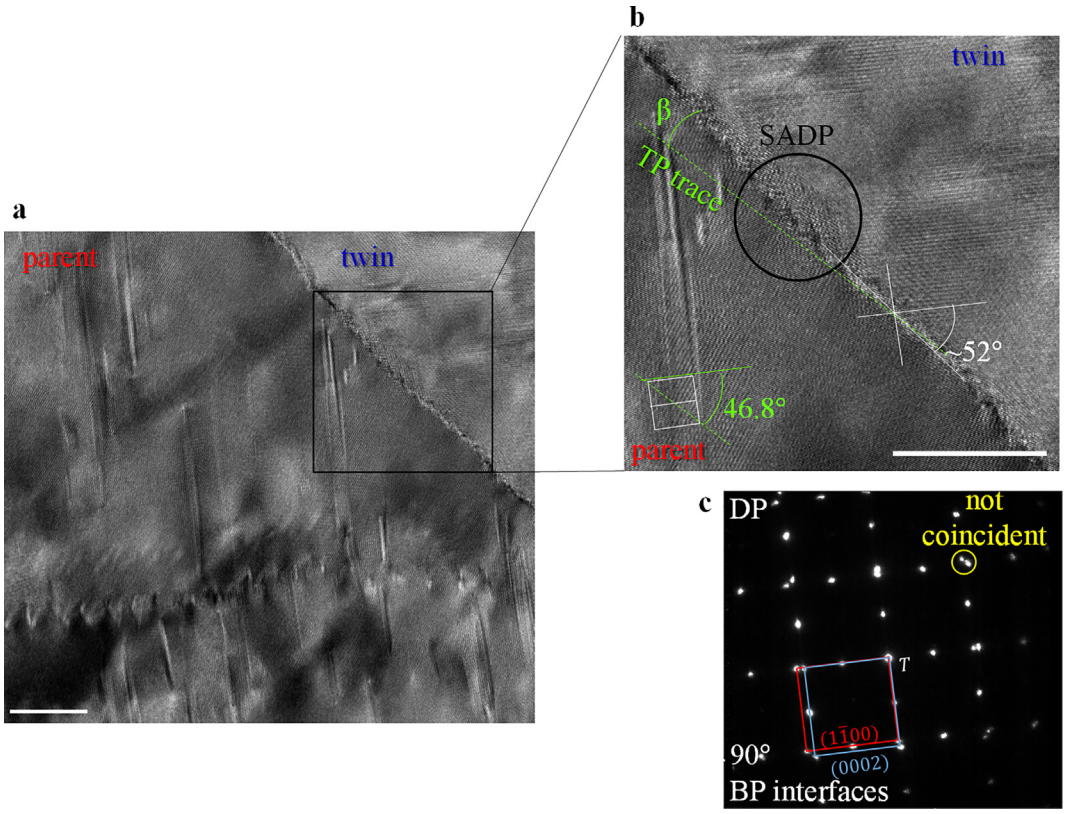

Fig. 8. Twin interfaces at high strain rates. (**a**) Bright Field TEM image of the parent and twin domains inside a compressed structure. (**b**) Magnification of a region of the TB showing a step–like configuration characterized by the presence of PB/BP serrations. The inclination of the TB does not coincide with what is expected for the invariant twin plane (denoted in the figure as TP). (**c**) SADP taken across the TB revealing that the {10$\bar{1}$2} diffraction spots are separated instead of overlapping with each other. A 90° lattice misorientation between the basal and prismatic plane of the twin and parent phases is thus established. All undefined scale bars correspond to 20 nm length.

interface evolves correspond to the ($\bar{5}$ $\bar{5}$1014) plane. By considering slight misalignment of the sample, this likely corresponds to the ($\bar{1}$ $\bar{1}$23) plane, 30° and 46.8° inclined in the *xy* and *yz* plane respectively. Very interestingly, the parent and twin crystals show overlapping projections in the {$\bar{1}$ $\bar{1}$23} PF (Fig. 10a). As the increase in strain rate may result in the activation of different twin modes [47], the misorientation, rotation axis, and the 3D geometry of the K_1 habit plane of other twin systems were investigated and compared to the characteristics of the twin in Regime II. However, by using the classical crystallographic theory of twinning [48] to predict possible twinning modes of type I, II, or compound, no clear correspondence was found. This implies that the changes in the twin shape can be addressed solely to a different (0$\bar{1}$12) twin process from Regime I to Regime II. Thus, although the twin habit plane does not coincide with the detected TB surface, the correspondence matrix ***C*** [1,49] (see supplementary discussion in Appendix A.1) related to the nucleated twins still corresponds to the one for (0$\bar{1}$12) twins. Nevertheless, a different way of accommodating the distortion must take place. It is worth noting that during the (0$\bar{1}$12) twinning process the (0$\bar{1}$12) plane remains fully invariant and no in–plane distortions occur (see supplementary discussion in Appendix A.1). Also, the ($\bar{1}$ $\bar{1}$23) is transformed into a plane of the same family in the twin domain (in general not true), i.e. the ($\bar{1}$2$\bar{1}$ $\bar{3}$), as reported in the PF (Fig. 10a). Here, however, in–plane distortions do occur (see supplementary discussion in Appendix A.1). Nevertheless, the shear direction remains invariant.

As simple consideration of twinning shear on the (0$\bar{1}$12) plane and associated shuffles do not suffice to fully describe the twin formed in Regime II, the overall twin shape must be the outcome of a competitive process dependent on the mobility of newly activated dislocations that accommodate the ($\bar{1}$ $\bar{1}$23)→($\bar{1}$2$\bar{1}$ $\bar{3}$) in–plane distortion. We remind that the only difference between Regime I and II is the increase in $\dot{\varepsilon}$. With the rise in strain rate, the higher applied speed of the indenter is accompanied by a faster response of the specimen that results in high axial compression stresses [50]. The latter becomes suitable for mobilizing the dislocations with the highest activation stress (Peierls stress) [51–53], i.e. < c + a > dislocations on the parent pyramidal planes [54,55]. In the *xy* plane, the lateral inclination of the upper TB (Fig. 9b) is close to that of ($\bar{1}$ $\bar{1}$22) slip plane (Fig. 10c), meaning that the activity of < c + a > dislocations on the ($\bar{1}$ $\bar{1}$22) pyramidal II order plane might have actively affected the twin mechanism. The competition of TDs and pyramidal slip (Fig. 10c, d) could therefore assist the ($\bar{1}$ $\bar{1}$23)→($\bar{1}$2$\bar{1}$ $\bar{3}$) in–plane lattice distortion, establishing a new parent–twin interface. As the twin nucleus expands, pyramidal slip activity provides a potential favorable strategy to facilitate and balance the lattice distortions generated at the TB during the twin propagation, resulting in an "unclassical" parent–twin interface. The rationale to the changes in the TB geometry may reside in an interfacial energy minimization via pyramidal slip activity. In a general but non-quantitative way, atomistic modellings were reported to agree with the continuum results indicating the feasibility of the pyramidal < c + a > dislocation–assisted twinning mechanism under an applied load [56]. In other words, the TB

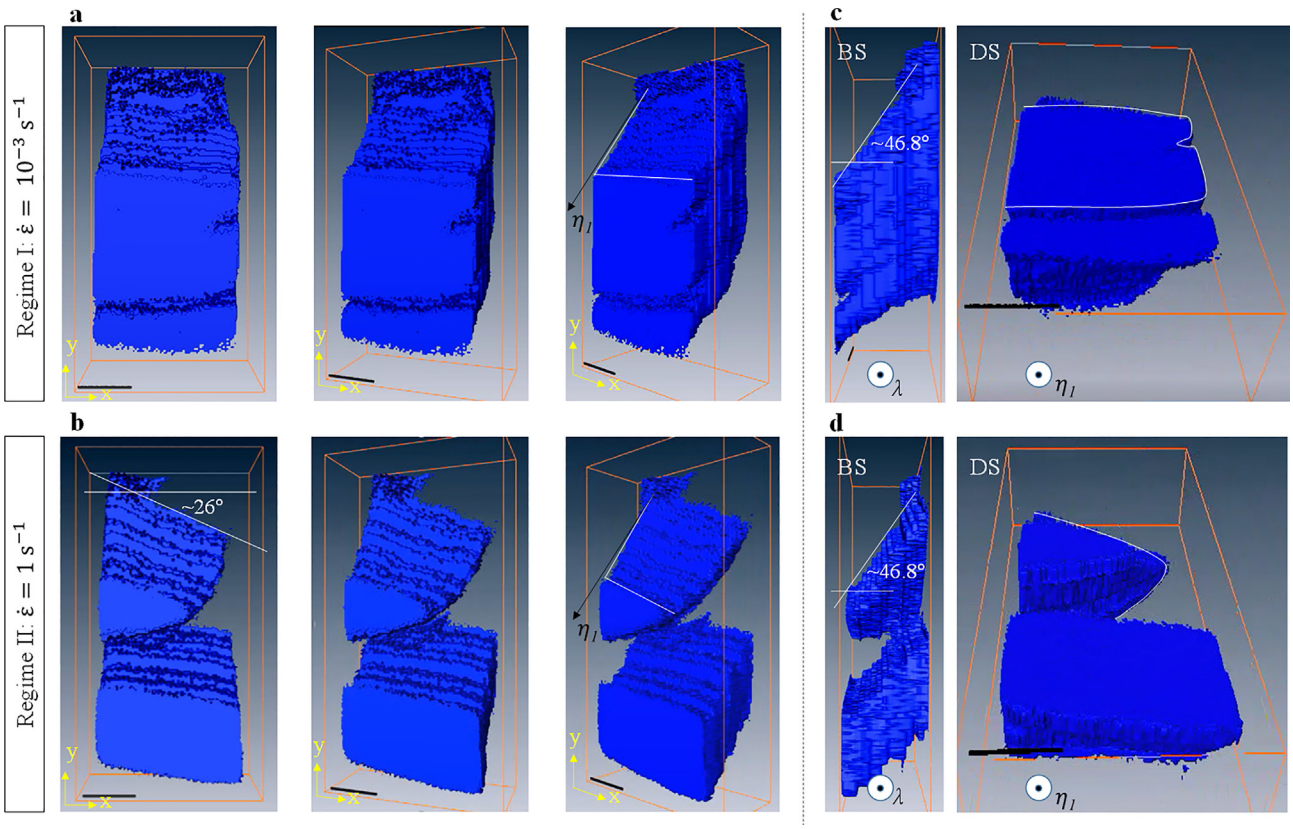

Fig. 9. Three–dimensional view of the twin domains in pillars deformed in (**a**) Regime I and (**b**) Regime II. (**c–d**) Bright Side (BS) and Dark Side (DS) views associated to the $(0\bar{1}12)$ twin, i.e. along $\lambda = [\bar{2}110]$ and $\eta_1 = [01\bar{1}1]$. All undefined scale bars correspond to 2 μm length.

develops along the plane containing the $[\bar{1}100]$ and $[01\bar{1}1]$ crystal directions (p and η_1), i.e. the $(\bar{1}\,\bar{1}23)$ plane (Fig. 10d). In support of this, the appearance of the "unclassical" TB is accompanied by a change in the strain rate sensitivity (SRS, m) and a reduction of the apparent activation volume (V^*) from 50 b_a^3 to 2 b_{c+a}^3 when < c + a > dislocations become mobile (see Paragraph 4.4 for details). The smaller activation volume suggests that the slip–assisted $(0\bar{1}12)$ twin growth by the aid of < c + a > dislocations becomes preferable and consequently prevalent under higher applied stress fields. Additionally, the growth perpendicular to the K_1 plane appears slower than along the other two directions of propagation, leading to the curved–like twin shape shown in Fig. 9b, schematically reproduced in Fig. 10b.

Now, the changes in the twin growth can be visible only thanks to the 3D reconstruction. Indeed, if one would solely investigate the BS view, the high–resolution (HR) TEM image (Fig. 10e, f) reveals that the forward twin propagation (along η_1) leads to semi–coherent TBs, i.e. mostly characterized by the alternation of PB/BP interfaces and coherent–TBs (CTB), as usually observed [57]. The investigation of the DS of the twin is hence crucial for understanding the twin process. This work, therefore, opens new aspects on DT that will require future experiments and simulations that focus on the precise atomic rearrangements not only in the BS view of the twin. So far, from our qualitative analysis, the appearance of the non–classical $(\bar{1}\,\bar{1}23)$ TB cannot be explained with the classical theory of twinning and we thus propose that < c + a > dislocations play a crucial role in accommodating the twin processes in HCP metals, allowing the $\{10\bar{1}2\}$ twin growth along a non–invariant twin plane. This work hence brings out new interpretations of some already reported anomalous twin features.

4.3. Twin mechanism at high strain rates

The detailed investigations performed on the developed twin domains of several pillars deformed in Regime III revealed that the majority of the TBs are characterized by PB/BP interfaces that establish a parent–twin lattice correspondence of 90° (Fig. 7 and Fig. 8). This induces to a deviation from the classical 86.4° misoriented interface [58]. In this configuration, unlike in Regime I and II, the $(0\bar{1}12)$ twin planes are not parallel in the twin and parent domains, as evidenced by the Selected Area Diffraction Pattern (SADP) acquired across the TB showing that the $(0\bar{1}12)$ diffraction spots are separated (Fig. 8c). Therefore, the classic rational crystallographic orientational mirror symmetry and consequently a crystallographic twin plane are no longer established. Additionally, the TB traces show an angular deviation (β) from the $(0\bar{1}12)$ twin plane that varies continuously (Fig. 8b and Fig. S.2). As the common axis between the two crystals coincides with the a–axis, a (90°, a) twin type forms. The latter was already reported in nano–pillar compressions at low strain rates (10^{-3} s^{-1}) and suggested to result from a prismatic–basal stacking rearrangement that takes place through a collective atomic movement eventually leading to a 90° reorientation of the HCP unit cell [18,59] (see Supplementary Fig. S.6).

At HSR, the accommodation of significant global strain must occur at the microscopic grain–scale within a very short time. Accordingly, different ways of accommodating the parent → twin transformation may occur under shock–loading compared to that under quasi–static conditions [59], requiring a more cooperative movement of a large number of atoms similar to a displacive–like transformation, as suggested by the increase in activation volume (see Paragraph 4.4). Recently it was observed that at low strain

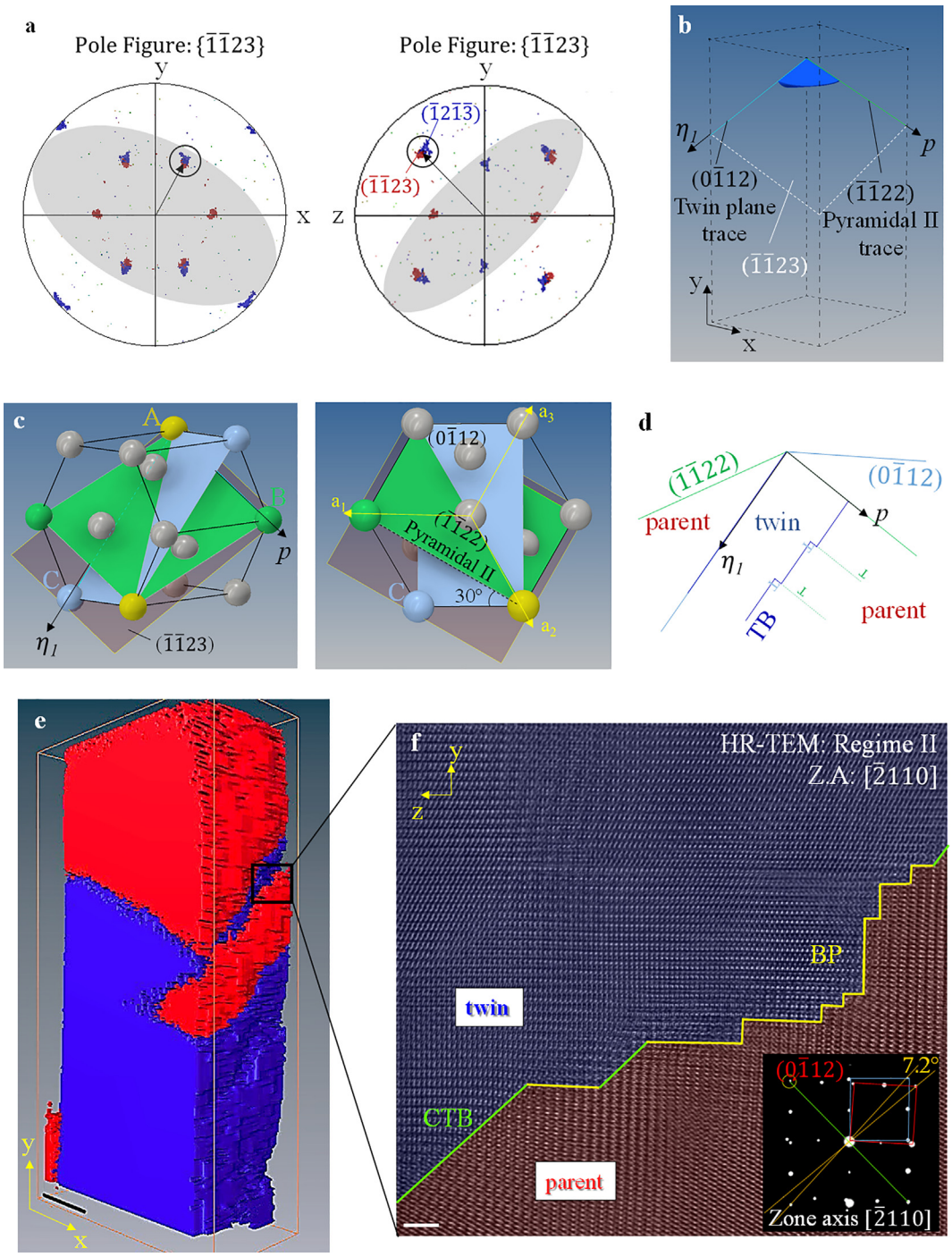

Fig. 10. (**a**) {$\bar{1}$ $\bar{1}$ 23} pole figures showing parent–twin projections. (**b**) Schematic reconstruction of the twin surface. (**c**) Representation of the (0 $\bar{1}$ 12) twin (blue), ($\bar{1}$ $\bar{1}$ 22) pyramidal II (green) and ($\bar{1}$ $\bar{1}$ 23) plane geometries. The latter intersects the atoms marked as A, B, and C. (**d**) TDs glide on the corresponding twin plane along η_1 inducing the lengthwise propagation. The lateral twin propagation is suspected to be mediated by < c + a > dislocations as *p* corresponds to a gliding direction of dislocations lying on the ($\bar{1}$ $\bar{1}$ 22) plane. (**e**) View of the three–dimensional parent–twin domains of a pillar deformed in Regime II. Scale bar, 2 μm (**f**) HR-TEM image from the [2 $\bar{1}$ 10] zone axis (also λ, thus BS view of the twin) illustrating a TB constituted by the alternation of PB/BP and CTB interfaces. The Selected Area Diffraction Pattern shows the (0 $\bar{1}$ 12) overlapping diffraction spots between the parent and the twin crystals establishing the crystallographic twin plane and the rational orientational relationship for {10 $\bar{1}$ 2} extension twin. Scale bar, 2 nm.

rates, but under high–stress conditions, the prismatic → basal plane conversion in Mg occurs only at the first stage of the twin process (twin embryo of few nm^3), leading to a 90° misoriented interface between the parent and twin lattices [19]. Subsequently, the twin propagation mechanism was reported to continue through the advancement of CTBs formed in a second stage by the rearrangement of dislocations at the PB/BP interfaces, re–establishing the classical lattice correspondence [19]. In this work, however, the TBs investigated belong to "adult" twins rather than embryonal. Thus, as the only difference from the other regimes lies in the applied $\dot{\varepsilon}$, our work confirms that the kinetically limited growth of {10 $\bar{1}$ 2} CTBs cannot accompany the imposed and required fast twin evolution. Consequently, at HSR the entire twin process appears to be adopted by prismatic → basal conversion.

The formation of TBs characterized by alternating PB/BP serrations with different segment lengths could explain the growth of incoherent TBs. Importantly, when gliding planes are nearly parallel between two neighboring misoriented grains, slip transmission for dislocations across TBs is easier and strongly affects the textural evolution of the material [60]. Stress concentrations at TB–slip interaction sites may be also more easily relieved, limiting pile-up stresses, multiple twin nucleation events and formation of cracks. Interactions of TBs comprised of PB/BP semi–coherent interfaces (90° between matrix and twin) would also influence the feasibility of twin–twin interpenetrations and formations of "double twins".

Now, PB/BP interfaces were already observed during shock loading in bulk Mg alloys [18,57]. However, in the case of bulk samples where a laterally "constrained" environment surrounds the twin domains, the interface strains generated by a 90° parent–twin misorientation are estimated to be too high and need to be reduced by a crystal rotation of 3.6° eventually leading to the invariant plane strain condition, not necessarily required in freestanding pillars. The unconventional (90°, *a*) and the conventional (86.4°, *a*) twins thus likely derive from the same initial distortion (see Appendix A.2) that takes place at the first stage of the twin mechanism, differing in a second stage only by a minor obliquity correction compensated by small lattice rotations [26]. It is worth reminding that the disconnections and disclinations are the dislocation arrays that locally accommodate respectively the translation and rotational parent–twin misfits at the twin boundary [61,62]. Therefore, the final character of the extension twin domains in bulk samples formed at HSR loading results from the cooperation of prismatic → basal transformation and subsequent rearrangement of interfacial defects, analogously to the dual–step mechanism recently observed in HCP metals [19], leading to parent-twin misorientation angles between 86.4° and 90°, as indeed recently confirmed in [63].

4.4. Strain rate sensitivity (SRS, m) and activation volume (V^*)

The changes in the material behavior can be observed also in the variations of SRS and V^* with

$$SRS = m = \frac{\partial \ln(\sigma_y)}{\partial \ln(\dot{\varepsilon})} \quad ; \quad V^* = \sqrt{3} K_B T \frac{\partial \ln(\dot{\varepsilon})}{\partial \sigma_y} \tag{1}$$

(where k_B is Boltzmann's constant) at the point of yield [64–67] (Fig. 11). As σ_y defines the onset of the plastic deformation, variations in the *SRS* and V^* are therefore expected to result from changes in the initial mechanism accommodating the plastic deformation.

For $\dot{\varepsilon} \leq 10^{-2} s^{-1}$, the applied low–speed deformation allows the development of complex strain fields beneath the tip–pillar contact region. As basal slip have the lowest τ_{CRSS} [68], their activation can be triggered even by small crystal deviations. The nucleation of twin embryos can be subsequently induced by the high–stress field at the defect sites such as dislocation pile-up and prior basal/prismatic dislocation slip activities [46], acting as a precursor to the formation of a stable twin nucleus [24]. We express therefore the activation volume of the incipient plasticity as 50 b_a^3. Despite the basal plane being parallel to the loading direction, small basal slip can also be activated inside the parent grain due to the bulging effect of the pillar. However, in the grains that have reoriented by twinning, the activation of < c + a > dislocations is favored [69], witnessed by the detected dislocation loops in Fig. 5.

At $10^{-2} s^{-1} < \dot{\varepsilon} < 10 s^{-1}$, the activation of < c + a > dislocations becomes possible due to the higher compressional stresses. The analysis of the BF and WBDF images reported in Fig. 6b–e shows indeed that, despite the lower achieved strain compared to Fig. 5, several < c + a > dislocation components have been activated. This is accompanied by a variation of the *SRS* (Fig. 11a), a reduction of the V^* to 2 b_{c+a}^3 (Fig. 11b) and a significant change in the spatial geometry of the lateral twin interface. The onset of the plastic deformation occurs through the twin nucleation mechanism (see Fig. 3), meaning that the activation of < c + a > dislocations plays a central role in accommodating the twin process. Additionally, in the process of severe plastic deformation, junction disclinations and other interface defects accumulated at the growing TB [62], such as interfacial dislocations associated with BP serrations [70,71], can act as a source for basal slip activity. Fig. 6b–e shows that the glide of these dislocations indeed occurs in the whole width of the parent grain, such that, with respect to the remaining matrix volume, basal slip are also still significant in Regime II. Additionally, the WBDF images of Fig. 6b–e show dotted–like diffraction contrasts lying on the basal plane, populating the parent grain. As recently reported [72,73], when leading partial dislocations of basal slip meet a pyramidal slip, sessile basal–pyramidal dislocation locks form generating puzzling diffraction contrasts, widely observed in Mg [6,33,74–76]. Also, the easy–glide pyramidal II < c + a > can undergo thermally activated, stress-dependent transitions into various lower-energy immobile product dislocations lying on basal planes [6]. These dislocation features, not visible in Regime I, suggest once more a substantial activity of < c + a > dislocations with increasing strain rate. As other twin modes predictable by the classical theory of twinning [48] do not reflect the characteristics of the twin observed in Regime II, the changes in the $\{10\bar{1}2\}$ twin mechanism from Regime I and II seem therefore attributed to the activation of < c + a > dislocations with the increase in strain rate.

While a significant increase in the σ_y is expected at higher strain rates [77,78], at $\dot{\varepsilon} \geq 10 s^{-1}$ the *SRS* decreases with the consequent increase in V^*. The hypothesis of softening induced by adiabatic heating seems not consistent as a higher amount of plastic work converted into heat is expected to lead to further subsequent softening, however not observed. This was instead explained by a further change in the characteristic of the growing twin interface described before. When the collective dislocation behavior becomes the major deformation mechanism for micron-sized samples, an increase in the activation volume is expected. In conclusion, the three different regimes can be distinguished by different deformation accommodations accompanying the twin mechanism. Regime I: multiple dislocations source; Regime II: single or surface dislocation source; Regime III: collective atomic movement.

5. Summary and conclusions

Our results, combined with previous findings [18,19], provide a closer observation on how the accommodation of the twin mechanism depends on both the applied stress condition and the kinetic compatibility of interfacial processes when a rapid rearrangement of the atom positions is externally imposed. The progressive evolution of the accommodating twin mechanisms from 10^{-4} s^{-1} to 500 s^{-1} has been extensively characterized. At low strain rates, the twin growth occurs along the invariant $(0\bar{1}12)$ twin plane by coherent twin boundaries migration according to the usual shear-shuffle mechanism. With increasing the strain rate though, the dislocation-assisted twin mechanism from dislocations with large Burgers vectors becomes favorable and consequently prevalent in Mg under higher applied stress field, allowing the evolution of the twin boundary along a crystallographic plane (here the $(\bar{1}\,\bar{1}23)$) that differs from the invariant extension twin plane. This suggest that deformation twinning would still be the major defor-

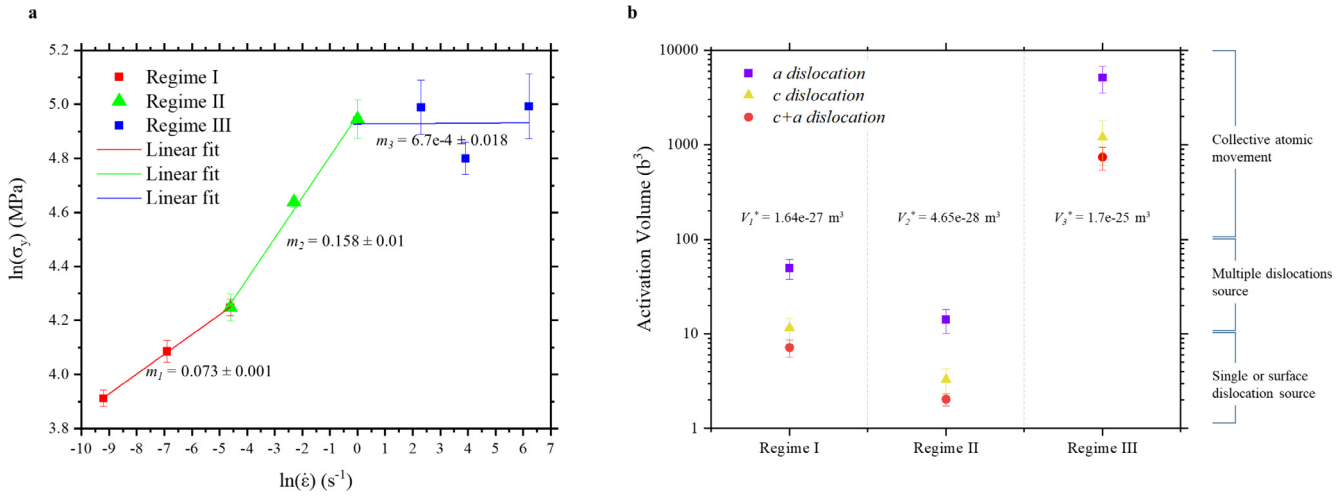

Fig. 11. (**a**) Variation of the strain rate sensitivity (SRS, m) value with strain rate. (**b**) Activation volumes in m^3 and as a function of b^3, with b being the magnitude of the different lattice dislocations in Mg.

mation carrier at room temperature even when the activity of non–basal slip is favored. We remind that the potential link or competition of deformation twinning with the dislocation activity is extremely crucial to better engineer Mg alloys for improving their ductility and hence extend the application ranges. At high strain rates, the kinetically limited parent → twin lattice rearrangement through dislocation motion requires that the twin mechanism is almost entirely accommodated by prismatic → basal conversion and the consequent advancement of basal/prismatic interfaces. A collective (but non–random) rearrangement of the atomic positions resulting in a 90° reorientation of the HCP crystal appears to entirely mediate the twin process, being naturally compatible with the required twin growth speed at high strain rates. The schematic of the initial and final atom positioning, recently proposed during prismatic → basal transformation [18], is illustrated in Supplementary Fig. S.6. The changes in the dynamic response and plastic accommodation mechanisms from low to high–speed deformation conditions in Mg at the micron–scale confirm that deformation twinning in HCP metals is not only stress– but also strongly time–controlled.

The occurrence of the different twinning accommodating processes in Mg depends solely on the local conditions of constraints. Our work shows that some of the recent interpretations deduced by particular twin morphologies are not universally valid. Being interpreted only by experimental evidence, our work adds new pieces to the fundamental comprehension of deformation twinning in HCP metals at the micron scale under unexplored loading regimes, aiming at closing the gap between currently reported atomistic simulations and macroscale high strain rate results. This study elicits future investigation on the different energy minimization twinning processes occurring at mid–high deformation rates, as well as the effect of size, temperature, grain boundaries, and solute addition during high strain rate deformations at the micron scale. The fact that at high strain rate the TB is composed of PB/BP semi–coherent interfaces (90° between matrix and twin) can have a large influence on the overall twinning behavior, as for instance during twin–twin interactions, or in "double–twins" formation, or additionally in detwinning which is particularly important under cycling loadings. At the micron–scale, this feature allows extended plasticity with no crack formation up to more than 10% strain, which is remarkable for such a material with limited ductility. This can have beneficial consequences for automotive, aeronautic or biomedical applications, where reliability and mechanical integrity under shock conditions are paramount. Extending the investigation to different crystal orientations and to polycrystalline samples would allow a broader understanding of how changes in the nature of the parent–twin interfaces influence the mechanical response of bulk Mg under high strain rate loadings.

CRediT authorship contribution statement

Nicolò M. della Ventura: Conceptualization, Methodology, Validation, Investigation, Data curation. **Amit Sharma:** Methodology, Validation, Investigation, Writing – review & editing. **Manish Jain:** Methodology, Investigation, Writing – review & editing. **Szilvia Kalácska:** Validation, Investigation, Writing – review & editing. **Thomas E.J. Edwards:** Methodology, Investigation, Writing – review & editing. **Cyril Cayron:** Conceptualization, Investigation, Writing – review & editing. **Roland Logé:** Project administration, Writing – review & editing. **Johann Michler:** Conceptualization, Resources, Investigation, Project administration, Validation, Writing – review & editing, Supervision. **Xavier Maeder:** Conceptualization, Methodology, Project administration, Resources, Investigation, Validation, Writing – review & editing, Supervision.

Declaration of Competing Interest

The authors declare that they have no known competing financial interests or personal relationships that could have appeared to influence the work reported in this paper.

Acknowledgements

The authors acknowledge financial support from the Swiss National Science Foundation (SNSF project numbers 200021_179011 and 206021_183328). The authors would like to thank the Scientific Center for Optical and Electron Microscopy ScopeM of the Swiss Federal Institute of Technology ETHZ. SzK and TEJE were supported by the EMPAPOSTDOCS-II program that has received funding from the European Union's Horizon 2020 research and innovation program under the Marie Sklodowska-Curie grant agreement number 754364.

Data availability

The data that support the findings of this study are available from the corresponding author upon reasonable request.

Appendix A

A.1 Crystallographic considerations during {10$\bar{1}$2} twinning process

To describe the process of extension twinning from a parent crystal p to its twin t, three matrices will be used: the distortion matrix **D**, the coordinate transformation matrix **T**, and the correspondence matrix **C** [49].

D $^{t} \rightarrow ^{p}$ gives the image x′ of a vector × by a linear distortion: x′ = D · x. The displacement field is given by x′ − x = (D-I) · x where I is the 3 × 3 identity matrix.

T $^{p} \rightarrow ^{t}$ allows the change of the coordinates of a fixed vector between the parent and twin bases: i.e. T $^{p} \rightarrow ^{t}$ = [$B^{p}_{hex} \rightarrow B^{t}_{hex}$].

C $^{t} \rightarrow ^{p}$ gives the images of the parent basis vectors by the distortion, i.e. a'_p, b'_p and c'_p, expressed in the twin basis, i.e. $(a'_p, b'_p, c'_p)_{/Bhex}{}^{t}$. These images are obtained from the coordinate transformation matrix and the distortion matrix: **C** $^{t} \rightarrow ^{p}$ = $(a'_p, b'_p, c'_p)^{t}_{/Bhex}$ = T $_{t} \rightarrow ^{p}$ $(a'_p, b'_p, c'_p)^{p}_{/Bhex}$ = T $^{t} \rightarrow ^{p}$ D $^{p} \rightarrow ^{t}$. The correspondence matrix is thus **C** $^{t} \rightarrow ^{p}$ = T $^{t} \rightarrow ^{p}$ D $^{p} \rightarrow ^{t}$, useful to calculate in the twin basis the coordinates of the image by the distortion of a vector written in the parent basis, i.e.:

$$x'^{t}_{/Bhex} = T^{t\rightarrow p} D^{p\rightarrow t} x^{p}_{/Bhex} = C^{t\rightarrow p} x^{p}_{/Bhex} \tag{A.1}$$

For further details, the reader is referred to Ref 24.

Based on this, the correspondence matrix of (0$\bar{1}$12) extension twin referred to the hcp coordinate system reported in Fig. 2a of the main text, will be:

$$\boldsymbol{C}^{t\rightarrow p,(0\bar{1}12)}_{hex} = \begin{pmatrix} 1 & -1/2 & 1 \\ 0 & 0 & 2 \\ 0 & 1/2 & 0 \end{pmatrix} \tag{A.2}$$

Note that the use of a 3 × 3 matrix requires necessarily the conversion from 4 to in 3–index notation. It can be checked that the $\mathbf{a_1} + 2\mathbf{a_2}$ of the parent crystal is transformed into the axis c of the twin, and the axis c of the parent is transformed into the axis $\mathbf{a_1} + 2\mathbf{a_2}$ of the twin (see also Fig. A.1):

$$\begin{bmatrix} 0 \\ 0 \\ 1 \end{bmatrix} = \begin{pmatrix} 1 & -1/2 & 1 \\ 0 & 0 & 2 \\ 0 & 1/2 & 0 \end{pmatrix} \begin{bmatrix} 1 \\ 2 \\ 0 \end{bmatrix}; \begin{bmatrix} 1 \\ 2 \\ 0 \end{bmatrix} = \begin{pmatrix} 1 & -1/2 & 1 \\ 0 & 0 & 2 \\ 0 & 1/2 & 0 \end{pmatrix} \begin{bmatrix} 0 \\ 0 \\ 1 \end{bmatrix} \tag{A.3}$$

Moreover, the global invariance of the (0$\bar{1}$12) twin plane (i.e. (0$\bar{1}$2) in 3–index notation) can be verified as follows:

$$\begin{bmatrix} h \\ k \\ l \end{bmatrix}_{/B^{t}_{hex}} = \boldsymbol{C}^{t\rightarrow p\,-T}_{hex} \begin{bmatrix} 0 \\ -1 \\ 2 \end{bmatrix}_{/B^{p}_{hex}} = \begin{pmatrix} 1 & 0 & 0 \\ -1/2 & 0 & 1/2 \\ 1 & 2 & 0 \end{pmatrix} \begin{bmatrix} 0 \\ -1 \\ 2 \end{bmatrix}_{/B^{p}_{hex}} = \begin{bmatrix} 0 \\ 1 \\ -2 \end{bmatrix}_{/B^{t}_{hex}} \tag{A.4}$$

Note that the mirror symmetry of the parent and twin lattices across the (0$\bar{1}$12) plane is also confirmed by the determinant of the correspondence matrix being −1. This implies the use of the right–hand rule for the parent and the left–hand rule for the twin coordinate systems (Fig. A.1). Moreover, the fact that the mirror plane corresponds to (0$\bar{1}$12) can be checked by using the coordinate transformation matrix.

The absence of in–plane distortion can be investigated by analyzing the images of two vectors initially lying along the twin plane, such as the [100] and the twinning shear direction [121].

$$\begin{bmatrix} u \\ v \\ w \end{bmatrix}_{/B^{t}_{hex}} = \begin{pmatrix} 1 & -1/2 & 1 \\ 0 & 0 & 2 \\ 0 & 1/2 & 0 \end{pmatrix} \begin{bmatrix} 1 \\ 0 \\ 0 \end{bmatrix}_{/B^{p}_{hex}} = \begin{bmatrix} 1 \\ 0 \\ 0 \end{bmatrix}_{/B^{t}_{hex}}; \quad \begin{bmatrix} u \\ v \\ w \end{bmatrix}_{/B^{t}_{hex}} = \begin{pmatrix} 1 & -1/2 & 1 \\ 0 & 0 & 2 \\ 0 & 1/2 & 0 \end{pmatrix} \begin{bmatrix} 1 \\ 2 \\ 1 \end{bmatrix}_{/B^{p}_{hex}} = \begin{bmatrix} 1 \\ 2 \\ 1 \end{bmatrix}_{/B^{t}_{hex}} \tag{A.5}$$

As the vectors lying along the twin plane remain invariant (image vector coincides with the vector in the parent basis), no in–plane distortion occurs during the twinning process.

During the extension twin process, the ($\bar{1}$ $\bar{1}$23) plane becomes the ($\bar{1}$2$\bar{1}$$\bar{3}$) plane in the twin basis:

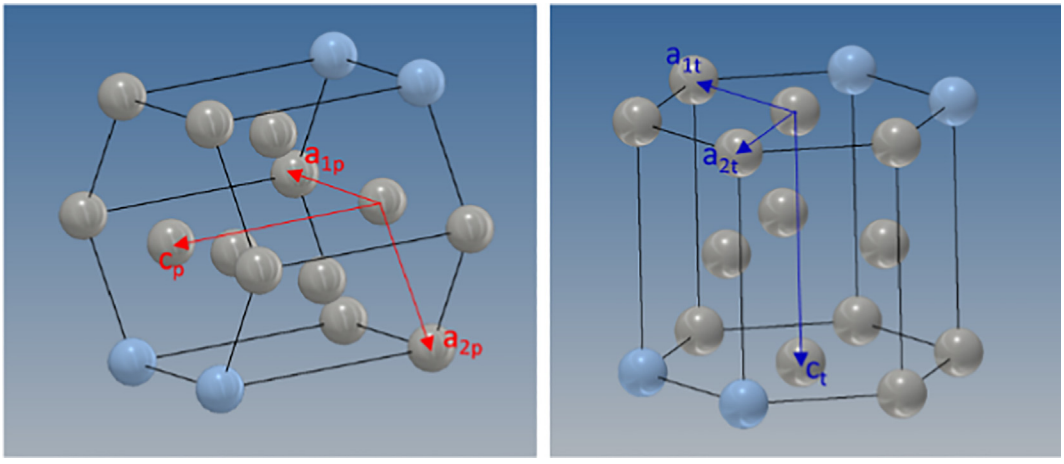

Fig. A1. Hexagonal coordinate systems for the parent and the twin crystals.

$$\begin{bmatrix} h \\ k \\ l \end{bmatrix}_{/B^t_{hex}} = \boldsymbol{C}^{t\to p^{-T}}_{hex} \begin{bmatrix} -1 \\ -1 \\ 3 \end{bmatrix}_{/B^p_{hex}} = \begin{pmatrix} 1 & 0 & 0 \\ -1/2 & 0 & 1/2 \\ 1 & 2 & 0 \end{pmatrix} \begin{bmatrix} -1 \\ -1 \\ 3 \end{bmatrix}_{/B^p_{hex}} = \begin{bmatrix} -1 \\ 2 \\ -3 \end{bmatrix}_{/B^t_{hex}} \quad (A.6)$$

Thus, the $(\bar{1}\ \bar{1}\ 23)_p$ plane is transformed into $(\bar{1}\,2\,\bar{1}\ \bar{3})_t$ (Fig. 10a, b of the main text), a plane of the same family, i.e. $\{\bar{1}\ \bar{1}\ 23\}$. In addition, contrarily to the $(0\,\bar{1}\,12)$ plane, in–plane distortion of the $(\bar{1}\ \bar{1}\ 23)_p$ plane occurs during extension twinning. Indeed, let us consider the image by correspondence of two directions in the plane, [1 2 1] and [–110].

$$\begin{bmatrix} u \\ v \\ w \end{bmatrix}_{/B^t_{hex}} = \begin{pmatrix} 1 & -1/2 & 1 \\ 0 & 0 & 2 \\ 0 & 1/2 & 0 \end{pmatrix} \begin{bmatrix} 1 \\ 2 \\ 1 \end{bmatrix}_{/B^p_{hex}} = \begin{bmatrix} 1 \\ 2 \\ 1 \end{bmatrix}_{/B^t_{hex}};$$
$$\begin{bmatrix} u \\ v \\ w \end{bmatrix}_{/B^t_{hex}} = \begin{pmatrix} 1 & -1/2 & 1 \\ 0 & 0 & 2 \\ 0 & 1/2 & 0 \end{pmatrix} \begin{bmatrix} -1 \\ 1 \\ 0 \end{bmatrix}_{/B^p_{hex}} = \begin{bmatrix} -3 \\ 0 \\ 1 \end{bmatrix}_{/B^t_{hex}} \quad (A.7)$$

The [1 2 1] is transformed into a direction of same family. By using the distortion matrix of Eq. (A.10), the reader can observe that additionally there is no rotation of this direction. The [1 2 1] direction (i.e. shear direction) is thus invariant. However, the $[\bar{1}\,10]$ direction is transformed into a direction of a different family, which proves that this does not remain invariant.

Interestingly, the parent–twin interface in Regime II develops along the $(\bar{1}\ \bar{1}\ 23)_p/(\bar{1}\,2\,\bar{1}\ \bar{3})_t$ plane. We conclude that the extension twin process might take place through the strain accommodation along the plane $(\bar{1}\ \bar{1}\ 23)$. As this occurs only at higher strain rates than those defined in Regime I, our current thinking is that the competition between the activated dislocations allows the accommodation of the $(\bar{1}\ \bar{1}\ 23)$ in–plane distortion. This however will require further dedicated investigations supported by challenging MD simulations aiming at analyzing the DS evolution of the twin.

A.2 Distortion matrices for (90°, *a*) twin and (86.4°)

The (90°, *a*) twin is very similar to the classical extension twin (86°, *a*). It has the same correspondence and only differs by a rotation of 3.6°. The coordinate transformation matrix $\mathbf{T}^{p\to t}$ and the distortion matrix $D^{p\to t}$ for (90°, *a*) twin associated with the chosen coordinate system are:

$$\boldsymbol{T}^{p\to t}_{hex} = \begin{pmatrix} 1 & -\frac{1}{2} & \frac{c}{a\sqrt{3}} \\ 0 & 0 & \frac{2c}{a\sqrt{3}} \\ 0 & \frac{a\sqrt{3}}{2c} & 0 \end{pmatrix} \quad and$$
$$\boldsymbol{D}^{p\to t,90^\circ}_{hex} = \boldsymbol{T}^{p\to t}_{hex}\boldsymbol{C}^{t\to p}_{hex} = \begin{pmatrix} 1 & -\frac{1}{2}+\frac{c}{2a\sqrt{3}} & 0 \\ 0 & \frac{c}{a\sqrt{3}} & 0 \\ 0 & 0 & \frac{a\sqrt{3}}{c} \end{pmatrix} \quad (A.8)$$

The distortion matrix associated with the (90°, *a*) twin can be mathematically associated to a pure stretch. $\boldsymbol{D}^{p\to t,90^\circ}_{hex}$ becomes indeed a symmetric matrix when transformed into orthonormal basis:

$$\boldsymbol{D}^{p\to t,90^\circ}_{ortho} = \boldsymbol{H}_{hex}\boldsymbol{D}^{p\to t,90^\circ}_{hex}\boldsymbol{H}^{-1}_{hex} \quad (A.9)$$

with $\boldsymbol{H}_{hex} = [\boldsymbol{B}_{ortho} \to \boldsymbol{B}_{hex}]$ the coordinate transformation matrix between the two bases. Note that $\boldsymbol{D}^{p\to t,90^\circ}_{hex}$ can usually also be reported as $\boldsymbol{U}^{p\to t}_{hex}$ in case of a pure crystal stretch.

The (90°, *a*) twin does not fulfill the classical invariant plane strain condition for the $(0\,\bar{1}\,12)$ plane of the classical extension twin (86°, *a*). The distortion matrix for this classical extension $(0\,\bar{1}\,12)$ twin can be however calculated by applying an obliquity correction that restores the invariant plane condition [26]. The distortion matrix that relates the parent and twin crystals when the process of $(0\,\bar{1}\,12)$ twin is completed would then be [26]:

$$\boldsymbol{D}^{p\to t,(0\,\bar{1}\,12)}_{hex} = \begin{pmatrix} 1 & \frac{1}{2}\left(\frac{17-17k^2+2k\sqrt{2-2k^2}}{\sqrt{17}\sqrt{17-16k^2+4k\sqrt{2-2k^2}}}-1\right) & \frac{\sqrt{3}kc}{2\sqrt{3}4a}\frac{\left(k+2\sqrt{2-2k^2}\right)}{\sqrt{17-16k^2+4k\sqrt{2-2k^2}}} \\ 0 & \frac{17-17k^2+2k\sqrt{2-2k^2}}{\sqrt{17}\sqrt{17-16k^2+4k\sqrt{2-2k^2}}} & \frac{\sqrt{3}kc}{\sqrt{3}4a}\frac{\left(k+2\sqrt{2-2k^2}\right)}{\sqrt{17-16k^2+4k\sqrt{2-2k^2}}} \\ 0 & -\frac{3\sqrt{3}a}{2\sqrt{17}c}\frac{k\sqrt{1-k^2}}{\sqrt{17-16k^2+4k\sqrt{2-2k^2}}} & \frac{68-64k^2+25k\sqrt{2-2k^2}}{4\sqrt{17}\sqrt{17-16k^2+4k\sqrt{2-2k^2}}} \end{pmatrix} \quad (A.10)$$

$$k = \sqrt{1-\frac{(c/a)^2}{3}}$$

The characteristic of the twin can be checked by calculating the rotation matrix $R^{p\to t}$ as:

$$\boldsymbol{R}^{p\to t} = \boldsymbol{H}^{o\to h}\boldsymbol{M}^{basal}\boldsymbol{D}^{p\to t,(0\,\bar{1}\,12)}_{hex}\left(\boldsymbol{C}^{t\to p}_{hex}\right)^{-1}\boldsymbol{H}^{h\to o} \quad (A.11)$$

where $\boldsymbol{M}^{basal}$ represents the mirror symmetry across the basal plane and $\boldsymbol{H}^{o\to h} = [B_{orto} \to B_{hex}]$ relates the orthonormal basis, with x–axis along the $-a_{1p}$ parent crystal direction, z–axis along the c direction and y–axis accordingly, to the hexagonal basis defined in Fig. A.1.

$$\boldsymbol{M}^{basal} = \begin{pmatrix} 1 & 0 & 0 \\ 0 & 1 & 0 \\ 0 & 0 & -1 \end{pmatrix} \boldsymbol{H}^{o\to h} = \begin{pmatrix} 1 & -\frac{1}{2} & 0 \\ 0 & \frac{\sqrt{3}}{2} & 0 \\ 0 & 0 & \frac{c}{a} \end{pmatrix} \quad (A.12)$$

One can check that the matrix $R^{p\to t}$ represents indeed an 86.4° rotation around the $[\bar{2}\,110]$ axis (same family as a-axis), as for the classical $(0\,\bar{1}\,12)$ twin.

By a dual step mechanism (pure stretch + obliquity correction), the classical $(0\,\bar{1}\,12)$ twin is therefore obtained. Hence, the unconventional (90°, *a*) (observed here) and the conventional (86.4°, *a*) twins (observed in bulk magnesium) resulting from high–speed loadings might derive from the same initial distortion matrix $\boldsymbol{D}^{p\to t,90^\circ}_{hex}$, differing only by a minor obliquity correction compensated by small lattice rotations. Differently from Ref. [26], here we do not specify the intermediate mechanism that induces the obliquity correction as this could take place through the aid of dislocations or being fully elastically accommodated. Identifying these intermediate mechanisms is extremely challenging due to the speed at which it occurs and would probably require complex in-situ TEM experiments.

Appendix B. Supplementary material

Supplementary data to this article can be found online at https://doi.org/10.1016/j.matdes.2022.110646.

References

[1] J.W. Christian, S. Mahajan, Deformation twinning, Prog. Mater. Sci. 39 (1-2) (1995) 1–157, https://doi.org/10.1016/0079-6425(94)00007-7.
[2] M.H. Yoo, J.K. Lee, Deformation twinning in h.c.p. metals and alloys, Philos. Mag. A Phys. Condens. Matter, Struct. Defects Mech. Prop. 63 (5) (1991) 987–1000, https://doi.org/10.1080/01418619108213931.
[3] M.H. Yoo, Slip, twinning, and fracture in hexagonal close-packed metals, Metall. Trans. A. 12 (3) (1981) 409–418, https://doi.org/10.1007/BF02648537.

[4] F. Yang, S.M. Yin, S.X. Li, Z.F. Zhang, Crack initiation mechanism of extruded AZ31 magnesium alloy in the very high cycle fatigue regime, Mater. Sci. Eng. A. 491 (1-2) (2008) 131–136, https://doi.org/10.1016/j.msea.2008.02.003.

[5] S.M. Yin, F. Yang, X.M. Yang, S.D. Wu, S.X. Li, G.Y. Li, The role of twinning-detwinning on fatigue fracture morphology of Mg-3%Al-1%Zn alloy, Mater. Sci. Eng. A. 494 (1-2) (2008) 397–400, https://doi.org/10.1016/j.msea.2008.04.056.

[6] Z. Wu, W.A. Curtin, The origins of high hardening and low ductility in magnesium, Nature. 526 (7571) (2015) 62–67, https://doi.org/10.1038/nature15364.

[7] I.J. Polmear, Recent developments in light alloys, Mater. Trans. JIM. 37 (1) (1996) 12–31, https://doi.org/10.2320/matertrans1989.37.12.

[8] I.J. Polmear, Magnesium alloys and applications, Mater. Sci. Technol. (United Kingdom) 10 (1) (1994) 1–16, https://doi.org/10.1179/mst.1994.10.1.1.

[9] A. Ostapovets, A. Serra, Review of non-classical features of deformation twinning in HCP metals and their description by disconnection mechanisms, Metals (Basel). 10 (2020) 1–20, https://doi.org/10.3390/met10091134.

[10] C. Cayron, Shifting the Shear Paradigm in the Crystallographic Models of Displacive Transformations in Metals and Alloys, Shifting the shear paradigm in the crystallographic models of displacive transformations in metals and alloys 8 (4) (2018) 181, https://doi.org/10.3390/cryst8040181.

[11] B. Li, E. Ma, Atomic shuffling dominated mechanism for deformation twinning in magnesium, Phys. Rev. Lett. 103 (3) (2009), https://doi.org/10.1103/PhysRevLett.103.035503.

[12] B. Li, X.Y. Zhang, Twinning with zero twinning shear, Scr. Mater. 125 (2016) 73–79, https://doi.org/10.1016/j.scriptamat.2016.07.004.

[13] A. Ostapovets, P. Molnár, On the relationship between the "shuffling-dominated" and "shear-dominated" mechanisms for 1 0 $\bar{1}$ 2 twinning in magnesium, Scr. Mater. 69 (2013) 287–290, https://doi.org/10.1016/j.scriptamat.2013.04.019.

[14] A. Serra, D.J. Bacon, R.C. Pond, Comment on "atomic shuffling dominated mechanism for deformation twinning in magnesium", Phys. Rev. Lett. 104 (2) (2010), https://doi.org/10.1103/PhysRevLett.104.029603.

[15] C. Cayron, R. Logé, Evidence of new twinning modes in magnesium questioning the shear paradigm, J. Appl. Crystallogr. 51 (3) (2018) 809–817, https://doi.org/10.1107/S160057671800567810.1107/S1600576718005678/nb5220sup1.pdf10.1107/S1600576718005678/nb5220sup2.nb.

[16] B. Xu, L. Capolungo, D. Rodney, On the importance of prismatic/basal interfaces in the growth of (1 0 $\bar{1}$ 2) twins in hexagonal close packed crystals, Scr. Mater. 68 (2013) 901–904, https://doi.org/10.1016/j.scriptamat.2013.02.023.

[17] A. Ostapovets, P. Molnár, R. Gröger, On basal-prismatic twinning interfaces in magnesium, IOP Conf. Ser. Mater. Sci. Eng. 63 (2014) 012134, https://doi.org/10.1088/1757-899X/63/1/012134.

[18] B.-Y. Liu, J. Wang, B. Li, L.u. Lu, X.-Y. Zhang, Z.-W. Shan, J.u. Li, C.-L. Jia, J. Sun, E. Ma, Twinning-like lattice reorientation without a crystallographic twinning plane, Nat. Commun. 5 (1) (2014), https://doi.org/10.1038/ncomms4297.

[19] Y. He, B. Li, C. Wang, S.X. Mao, Direct observation of dual-step twinning nucleation in hexagonal close-packed crystals, Nat. Commun. 11 (1) (2020), https://doi.org/10.1038/s41467-020-16351-0.

[20] M.R. Barnett, Z. Keshavarz, A.G. Beer, X. Ma, Non-Schmid behaviour during secondary twinning in a polycrystalline magnesium alloy, Acta Mater. 56 (1) (2008) 5–15, https://doi.org/10.1016/j.actamat.2007.08.034.

[21] X.Y. Zhang, B. Li, X.L. Wu, Y.T. Zhu, Q. Ma, Q. Liu, P.T. Wang, M.F. Horstemeyer, Twin boundaries showing very large deviations from the twinning plane, Scr. Mater. 67 (10) (2012) 862–865, https://doi.org/10.1016/j.scriptamat.2012.08.012.

[22] H.A. Khater, A. Serra, R.C. Pond, Atomic shearing and shuffling accompanying the motion of twinning disconnections in Zirconium, Philos. Mag. 93 (10-12) (2013) 1279–1298, https://doi.org/10.1080/14786435.2013.769071.

[23] J. Wang, L. Liu, C.N. Tomé, S.X. Mao, S.K. Gong, Twinning and de-twinning via glide and climb of twinning dislocations along serrated coherent twin boundaries in hexagonal-close-packed metals, Mater. Res. Lett. 1 (2) (2013) 81–88, https://doi.org/10.1080/21663831.2013.779601.

[24] L. Capolungo, I.J. Beyerlein, Nucleation and stability of twins in hcp metals, Phys. Rev. B - Condens. Matter Mater. Phys. 78 (2008) 1–19, https://doi.org/10.1103/PhysRevB.78.024117.

[25] S. Mendelson, Dislocation dissociations in hcp metals, J. Appl. Phys. 41 (5) (1970) 1893–1910, https://doi.org/10.1063/1.1659139.

[26] C. Cayron, Hard-sphere displacive model of extension twinning in magnesium, Mater. Des. 119 (2017) 361–375, https://doi.org/10.1016/j.matdes.2017.01.047.

[27] G. Guillonneau, M. Mieszala, J. Wehrs, J. Schwiedrzik, S. Grop, D. Frey, L. Philippe, J.M. Breguet, J. Michler, J.M. Wheeler, Nanomechanical testing at high strain rates: new instrumentation for nanoindentation and microcompression, Mater. Des. 148 (2018) 39–48, https://doi.org/10.1016/j.matdes.2018.03.050.

[28] S. Kalácska, Z. Dankházi, G. Zilahi, X. Maeder, J. Michler, P.D. Ispánovity, I. Groma, Investigation of geometrically necessary dislocation structures in compressed Cu micropillars by 3-dimensional HR-EBSD, Mater. Sci. Eng. A. 770 (2020) 138499, https://doi.org/10.1016/j.msea.2019.138499.

[29] N.M. Della Ventura, S. Kalácska, D. Casari, T.E.J. Edwards, A. Sharma, J. Michler, R. Logé, X. Maeder, {10$\bar{1}$2} twinning mechanism during in situ micro-tensile loading of pure Mg: Role of basal slip and twin-twin interactions, Mater. Des. 197 (2021). https://doi.org/10.1016/j.matdes.2020.109206.

[30] M.R. Barnett, Twinning and the ductility of magnesium alloys. Part I: "Tension" twins, Mater. Sci. Eng. A. 464 (1-2) (2007) 1–7, https://doi.org/10.1016/j.msea.2006.12.037.

[31] K.E. Prasad, K. Rajesh, U. Ramamurty, Micropillar and macropillar compression responses of magnesium single crystals oriented for single slip or extension twinning, Acta Mater. 65 (2014) 316–325, https://doi.org/10.1016/j.actamat.2013.10.073.

[32] A. Chapuis, J.H. Driver, Temperature dependency of slip and twinning in plane strain compressed magnesium single crystals, Acta Mater. 59 (5) (2011) 1986–1994, https://doi.org/10.1016/j.actamat.2010.11.064.

[33] C.M. Byer, B. Li, B. Cao, K.T. Ramesh, Microcompression of single-crystal magnesium, Scr. Mater. 62 (8) (2010) 536–539, https://doi.org/10.1016/j.scriptamat.2009.12.017.

[34] T. Nogaret, W.A. Curtin, J.A. Yasi, L.G. Hector, D.R. Trinkle, Atomistic study of edge and screw (c + a) dislocations in magnesium, Acta Mater. 58 (13) (2010) 4332–4343, https://doi.org/10.1016/j.actamat.2010.04.022.

[35] K. Máthis, M. Knapek, F. Šiška, P. Harcuba, D. Ugi, P.D. Ispánovity, I. Groma, K.S. Shin, On the dynamics of twinning in magnesium micropillars, Mater. Des. 203 (2021) 109563, https://doi.org/10.1016/j.matdes.2021.109563.

[36] N. Rohbeck, R. Ramachandramoorthy, D. Casari, P. Schürch, T.E.J. Edwards, L. Schilinsky, L. Philippe, J. Schwiedrzik, J. Michler, Effect of high strain rates and temperature on the micromechanical properties of 3D-printed polymer structures made by two-photon lithography, Mater. Des. 195 (2020) 108977, https://doi.org/10.1016/j.matdes.2020.108977.

[37] R. Ramachandramoorthy, J. Schwiedrzik, L. Petho, C. Guerra-Nuñez, D. Frey, J.-M. Breguet, J. Michler, Dynamic Plasticity and Failure of Microscale Glass: Rate-Dependent Ductile-Brittle-Ductile Transition, Nano Lett. 19 (4) (2019) 2350–2359, https://doi.org/10.1021/acs.nanolett.8b0502410.1021/acs.nanolett.8b05024.s001.

[38] R. Ramachandramoorthy, W. Gao, R. Bernal, H. Espinosa, High Strain Rate Tensile Testing of Silver Nanowires: Rate-Dependent Brittle-to-Ductile Transition, Nano Lett. 16 (1) (2016) 255–263, https://doi.org/10.1021/acs.nanolett.5b0363010.1021/acs.nanolett.5b03630.s001.

[39] Y. Liu, N. Li, S. Shao, M. Gong, J. Wang, R.J. McCabe, Y. Jiang, C.N. Tomé, Characterizing the boundary lateral to the shear direction of deformation twins in magnesium, Nat. Commun. 7 (1) (2016), https://doi.org/10.1038/ncomms11577.

[40] A. Fernández, A. Jérusalem, I. Gutiérrez-Urrutia, M.T. Pérez-Prado, Three-dimensional investigation of grain boundary-twin interactions in a Mg AZ31 alloy by electron backscatter diffraction and continuum modeling, Acta Mater. 61 (20) (2013) 7679–7692, https://doi.org/10.1016/j.actamat.2013.09.005.

[41] A. Luque, M. Ghazisaeidi, W.A. Curtin, A new mechanism for twin growth in Mg alloys, Acta Mater. 81 (2014) 442–456, https://doi.org/10.1016/j.actamat.2014.08.052.

[42] C. Zhang, H. Li, P. Eisenlohr, W. Liu, C.J. Boehlert, M.A. Crimp, T.R. Bieler, Effect of realistic 3D microstructure in crystal plasticity finite element analysis of polycrystalline Ti-5Al-2.5Sn, Int. J. Plast. 69 (2015) 21–35, https://doi.org/10.1016/j.ijplas.2015.01.003.

[43] S. Wang, M. Gong, R.J. McCabe, L. Capolungo, J. Wang, C.N. Tomé, Characteristic boundaries associated with three-dimensional twins in hexagonal metals, Sci. Adv. 6 (28) (2020), https://doi.org/10.1126/sciadv.aaz2600.

[44] Y. Liu, P.Z. Tang, M.Y. Gong, R.J. McCabe, J. Wang, C.N. Tomé, Three-dimensional character of the deformation twin in magnesium, Nat. Commun. 10 (1) (2019), https://doi.org/10.1038/s41467-019-10573-7.

[45] N. Dixit, K.Y. Xie, K.J. Hemker, K.T. Ramesh, Microstructural evolution of pure magnesium under high strain rate loading, Acta Mater. 87 (2015) 56–67, https://doi.org/10.1016/j.actamat.2014.12.030.

[46] J. Jeong, M. Alfreider, R. Konetschnik, D. Kiener, S.H. Oh, In-situ TEM observation of 10$\bar{1}$2 twin-dominated deformation of Mg pillars: twinning mechanism, size effects and rate dependency, Acta Mater. 158 (2018) 407–421, https://doi.org/10.1016/j.actamat.2018.07.027.

[47] R.C. Pond, J.P. Hirth, Topological model of type II deformation twinning, Acta Mater. 151 (2018) 229–242, https://doi.org/10.1016/j.actamat.2018.03.014.

[48] The theory of the crystallography of deformation twinning, Proc. R. Soc. London. Ser. A. Math. Phys. Sci. 288 (1965) 240–255. https://doi.org/10.1098/rspa.1965.0216

[49] C. Cayron, The transformation matrices (Distortion, orientation, correspondence), their continuous forms and their variants, Acta Crystallogr. Sect. A Found. Adv. 75 (2019) 411–437, https://doi.org/10.1107/S205327331900038X.

[50] R.W. Armstrong, S.M. Walley, High strain rate properties of metals and alloys, Int. Mater. Rev. 53 (3) (2008) 105–128, https://doi.org/10.1179/174328008X277795.

[51] Y. Tang, J.A. El-Awady, Formation and slip of pyramidal dislocations in hexagonal close-packed magnesium single crystals, Acta Mater. 71 (2014) 319–332, https://doi.org/10.1016/j.actamat.2014.03.022.

[52] R.E. Reed-Hill, W.D. Robertson, Deformation of magnesium single crystals by nonbasal slip, Jom. 9 (4) (1957) 496–502.

[53] H. Yoshinaga, R. Horiuchi, On the Nonbasal Slip in Magnesium Crystals, Trans. Japan Inst. Met. 5 (1) (1964) 14–21, https://doi.org/10.2320/matertrans1960.5.14.

[54] H. Tonda, K. Nakamura, K. Takashima, {1122}⟨1123⟩ Slip in Magnesium Single Crystal, J. Japan Inst. Light Met. 42 (1992) 765–771, https://doi.org/10.2464/jilm.42.765.

[55] H. Fan, J.A. El-Awady, Towards resolving the anonymity of pyramidal slip in magnesium, Mater. Sci. Eng. A. 644 (2015) 318–324, https://doi.org/10.1016/j.msea.2015.07.080.

[56] M. Ghazisaeidi, W.A. Curtin, Analysis of dissociation of ⟨c⟩ and ⟨c + a⟩ dislocations to nucleate (1 01 2) twins in Mg, Model. Simul. Mater. Sci. Eng. 21 (2013), https://doi.org/10.1088/0965-0393/21/5/055007.
[57] K. Dang, S. Wang, M. Gong, R.J. McCabe, J. Wang, L. Capolungo, Formation and stability of long basal-prismatic facets in Mg, Acta Mater. 185 (2020) 119–128, https://doi.org/10.1016/j.actamat.2019.11.070.
[58] M. Niewczas, Lattice correspondence during twinning in hexagonal close-packed crystals, Acta Mater. 58 (17) (2010) 5848–5857, https://doi.org/10.1016/j.actamat.2010.06.059.
[59] H. Zong, X. Ding, T. Lookman, J.u. Li, J. Sun, E.K. Cerreta, J.P. Escobedo, F.L. Addessio, C.A. Bronkhorst, Collective nature of plasticity in mediating phase transformation under shock compression, Phys. Rev. B - Condens. Matter Mater. Phys. 89 (22) (2014), https://doi.org/10.1103/PhysRevB.89.220101.
[60] Q. Yu, J. Wang, Y. Jiang, R.J. McCabe, N. Li, C.N. Tomé, Twin-twin interactions in magnesium, Acta Mater. 77 (2014) 28–42, https://doi.org/10.1016/j.actamat.2014.05.030.
[61] A.E. Romanov, A.L. Kolesnikova, Application of disclination concept to solid structures, Prog. Mater. Sci. 54 (6) (2009) 740–769, https://doi.org/10.1016/j.pmatsci.2009.03.002.
[62] C.D. Barrett, H. El Kadiri, The roles of grain boundary dislocations and disclinations in the nucleation of 1 0 1 2 twinning, Acta Mater. 63 (2014) 1–15, https://doi.org/10.1016/j.actamat.2013.09.012.
[63] K.Y. Xie, K. Hazeli, N. Dixit, L. Ma, K.T. Ramesh, K.J. Hemker, Twin boundary migration mechanisms in quasi-statically compressed and plate-impacted mg single crystals, Sci. Adv. 7 (42) (2021), https://doi.org/10.1126/sciadv.abg3443.
[64] Q. Wei, S. Cheng, K.T. Ramesh, E. Ma, Effect of nanocrystalline and ultrafine grain sizes on the strain rate sensitivity and activation volume: Fcc versus bcc metals, Mater. Sci. Eng. A. 381 (1-2) (2004) 71–79, https://doi.org/10.1016/j.msea.2004.03.064.
[65] Y.F. Shen, L. Lu, M. Dao, S. Suresh, Strain rate sensitivity of Cu with nanoscale twins, Scr. Mater. 55 (4) (2006) 319–322, https://doi.org/10.1016/j.scriptamat.2006.04.046.
[66] J.M. Wheeler, V. Maier, K. Durst, M. Göken, J. Michler, Activation parameters for deformation of ultrafine-grained aluminium as determined by indentation strain rate jumps at elevated temperature, Mater. Sci. Eng. A. 585 (2013) 108–113, https://doi.org/10.1016/j.msea.2013.07.033.
[67] E.W. Hart, Theory of the tensile test, Acta Metall. 15 (2) (1967) 351–355, https://doi.org/10.1016/0001-6160(67)90211-8.
[68] H. Conrad, W.D. Robertson, Effect of temperature on the flow stress and strain-hardening coefficient of magnesium single crystals, Jom. 9 (4) (1957) 503–512.
[69] F. Wang, S.R. Agnew, Dislocation transmutation by tension twinning in magnesium alloy AZ31, Int. J. Plast. 81 (2016) 63–86, https://doi.org/10.1016/j.ijplas.2016.01.012.
[70] J.P. Hirth, J. Wang, C.N. Tomé, Disconnections and other defects associated with twin interfaces, Prog. Mater. Sci. 83 (2016) 417–471, https://doi.org/10.1016/j.pmatsci.2016.07.003.
[71] M. Gong, J.P. Hirth, Y. Liu, Y. Shen, J. Wang, Interface structures and twinning mechanisms of twins in hexagonal metals, Mater. Res. Lett. 5 (7) (2017) 449–464, https://doi.org/10.1080/21663831.2017.1336496.
[72] B. Li, Q.W. Zhang, S.N. Mathaudhu, Basal-pyramidal dislocation lock in deformed magnesium, Scr. Mater. 134 (2017) 37–41, https://doi.org/10.1016/j.scriptamat.2017.02.040.
[73] N. Bertin, C.N. Tomé, I.J. Beyerlein, M.R. Barnett, L. Capolungo, On the strength of dislocation interactions and their effect on latent hardening in pure Magnesium, Int. J. Plast. 62 (2014) 72–92, https://doi.org/10.1016/j.ijplas.2014.06.010.
[74] B. Syed, J. Geng, R.K. Mishra, K.S. Kumar, [0 0 0 1] Compression response at room temperature of single-crystal magnesium, Scr. Mater. 67 (7-8) (2012) 700–703, https://doi.org/10.1016/j.scriptamat.2012.06.036.
[75] H. Tonda, S. Ando, Effect of temperature and shear direction on yield stress by {1122}⟨1123⟩ slip in HCP metals, in: Metall. Mater. Trans. A Phys. Metall. Mater. Sci., 2002: pp. 831–836. https://doi.org/10.1007/s11661-002-0152-z.
[76] S. Ando, H. Tonda, Non-basal slips in magnesium and magnesium-lithium alloy single crystals, Mater. Sci. Forum. 350 (2000) 43–48, https://doi.org/10.4028/www.scientific.net/msf.350-351.43.
[77] S. Breumier, S. Sao-Joao, A. Villani, M. Lévesque, G. Kermouche, High strain rate micro-compression for crystal plasticity constitutive law parameters identification, Mater. Des. 193 (2020) 108789, https://doi.org/10.1016/j.matdes.2020.108789.
[78] Z.Y. Liang, X. Wang, W. Huang, M.X. Huang, Strain rate sensitivity and evolution of dislocations and twins in a twinning-induced plasticity steel, Acta Mater. 88 (2015) 170–179, https://doi.org/10.1016/j.actamat.2015.01.013.